International Journal for Computational Methods in Engineering Science & Mechanics (USA)

https://www.tandfonline.com/toc/ucme20/current

Accepted May 5th 2023

COMPUTATION OF STAGNATION FLOW OF MAGNETITE/COBALT/ MANGANESE-ZINC-AQUEOUS NANO-FERROFLUIDS FROM A STRETCHING SHEET WITH MAGNETIC INDUCTION EFFECTS

M. Ferdows[1], Tahia Tazin[2], O. Anwar Bég[3], T.A. Bég[4] and Ali Kadir[3]

[1]*Research Group of Fluid Flow Modeling and Simulation, Department of Applied Mathematics, University of Dhaka,* ***Bangladesh.***
[2]*Department of Mathematics, Comilla University, Comilla,3506, Bangladesh.*
[3]*MPESG, Department of Mechanical/Aeronautical Engineering, SEE, Salford University, Manchester, M54WT,* ***UK****.*
[4]*Renewable Energy and Computational Multi-Physics, Israfil House, Dickenson Rd., M13,* ***UK.***

**Correspondence to: ferdows@du.ac.bd*

ABSTRACT:

A theoretical study is presented for the steady magnetohydrodynamic (MHD) boundary layer stagnation point flow of a nano-ferrofluid along a linearly moving stretching sheet, as a simulation of functional magnetic materials processing. Due to having emerging applications in heat transfer, the nano-ferrofluids draw the attention which comprises an aqueous base fluid doped with a variety of magnetic nanoparticles i. e. magnetite (Fe_3O_4), cobalt ferrite ($CoFe_2O_4$) and Manganese-Zinc (Mn-Zn) ferrite. A partial differential equation mathematical model is developed for mass, momentum, magnetic field continuity (induction) and energy with appropriate wall and free stream boundary conditions. Following similarity transformations, the dimensionless resultant nonlinear ordinary differential boundary value problem is solved numerically using the robust bvp4c function in MATLAB which features very efficient 4th order optimized Runge-Kutta quadrature. Dual solutions for the upper branch and lower branch separated by a critical point are identified. Visualization of velocity, temperature and induced magnetic field function are presented graphically including validation of solutions with previous studies. Furthermore skin-friction coefficient and the local Nusselt number are also computed. The impact of the controlling parameters i. e. Prandtl number ($Pr = 6.2$), nanoparticle volume fraction parameter ($0.01 \leq \varphi \leq 0.1$), reciprocal of magnetic Prandtl number ($2 \leq \lambda \leq 10$), magnetic parameter ($0.01 \leq \beta \leq 0.9$) and stretching rate ratio parameter ($0.5 \leq A \leq 1.5$) have been illustrated through graphs and evaluated when a desire heat transfer can occur. Furthermore, resistance between fluid and the plate can be increased with the growing magnetic prandtl number values. Increment in magnetic parameter (β) produces an elevation in the induced magnetic field magnitudes. Skin friction and Nusselt number are found to be greater for cobalt nanoparticles when compared to magnetite and Mn-Zn ferromagnetic nanoparticles when there is an increase in reciprocal magnetic Prandtl

number. The simulations provide a deeper insight into the manufacturing flows of functional nano-ferromagnetic materials of relevance to deposition and coating systems.

KEYWORDS: *Ferromagnetic fluids, stagnation flow. Boundary layers, magnetic induction, magnetite (Fe_3O_4), cobalt (Co), Manganese-Zinc (Mn-Zn) nanoparticles, MATLAB, stretching sheet, local Nusselt number.*

1.INTRODUCTION:

Applications of functional magnetic liquids and ferrofluids have recently attracted significant interest in manufacturing systems [1], coating designs with functional materials [2] and surface finishing [3] for enhanced durability of engineering components. These intelligent materials offer significant advantages for corrosion protection, coating film consistency and adaptability in extreme environments [4]. Increasingly they are being engineered with nanoparticles [5] to provide more stability and more strategic deployment in the aerospace, marine, biomedical and environmental sectors. Boundary layers are fundamental to the manufacturing of coatings and frequently feature *stagnation point flows* wherein the impinging coating material is deposited in a controlled fashion on the substrate to achieve more precise distribution and consistency [6, 7]. Stagnation flows may be normal or oblique in nature. Other applications include optical engineering [8], chemical engineering [9] and blade surfacing [10]. Hiemenz [11] initiated the study of boundary layer stagnation flows, deriving analytical solutions for two-dimensional stagnation point flow over a flat plate (horizontal wall). Sparrow and Cess [12] generalized the Hiemenz theory to consider heat transfer and thermal boundary layers. Gorla [13] investigated magnetohydrodynamic non-Newtonian stagnation point flow.

In the 21st century, nanotechnology has emerged as a significant development. It features materials and systems engineered at the nanoscale for enhanced functionality and efficiency and also precision manipulation for specific applications. Nanofluids are offered to enhance the thermal performance of ordinary fluids [14]. Some commonly used fluids, namely, water, kerosene, ethylene glycol and mineral oils exhibit inferior thermal performance, compared with metals, non-metallic (carbon-based) and hybrid metallic/carbon nanofluid. Sreedevi et al. [15] have investigated the effect of convective boundary condition on heat and mass transfer of nanofluid flow over a thin needle filled with carbon nanotubes. Later, they have used Maxwell hybrid nanofluid for discussing the effect of Cattaneo–Christov heat flux on heat and mass transfer characteristics of flow over stretching/shrinking sheet [16]. Ferdows et al. [17] analyzed the effect magnetics induction on Hiemenz flow of carbon nanotubes (CNT) where dual solution of electro conductive single walled CNTs and multi walled CNT have been observed. Magnetic nanofluids and ferromagnetic nanofluids offer the simultaneous benefits of improved thermal efficiency and also functionality i. e. tunability [18, 19]. In the simulation of such fluids, viscous, nanoscale and magnetohydrodynamic (MHD) effects must be considered simultaneously. Important MHD phenomena are ferromagnetism, magnetic induction, dipole and quadrupole magnetism. This has motivated a number of researchers to examine ferromagnetic nanofluid dynamics in materials processing, where models provide a powerful insight into flow characteristics and act as a useful compliment to laboratory-based studies. Many different applications have been explored including coatings, tribology, thermal ducts and power generation. Entropy generation and heat transfer analysis inside a square cavity for various hybrid nanofluids (alumina and carbon nanotubes based and magnetic nanofluids) with thermal radiation have been analyzed by Sreedevi et al. [20-22]. Bahirael and Hangi [23] investigated the impact of quadrupole magnetic field on performance of the nanofluid containing Mn–Zn ferrite nanoparticles in a counter-flow double-pipe heat exchanger. In another paper, Bahirael *et al.* [24] studied Mn-Zn ferrite-water ferrofluid flow through an annulus under the influence of non-uniform magnetic field, noting that the velocity profile becomes flatter at the cross section of the annulus and a strong increase in both convective heat transfer coefficient and pressure drop with stronger magnetic field. Other studies include Aneja *et al.* [25] (on non-uniform magnetic field effects on bio-nanofluid coatings), Azizian et al. [26] (on magnetite nanofluid boundary layers), Umavathi *et al*. [27] (on time-dependent ferromagnetic nanofluid tribological squeezing flow and heat transfer), Ferdows and Alzahrani [28] (on non-isothermal ferromagnetic nanofluid flow with induced magnetic field effects), Reddy *et al.* [29] (on buoyancy-driven coating flow using magnetic nanofluids with Hall current and ion slip effects), Al-Kouz et al. [30] (on second law thermodynamic optimization of water-Fe_3O_4/CNT hybrid magnetic nanofluid flow in a permeable medium-based trapezoidal wavy enclosure), Reddy el al. [31] (on the heat transfer of MgO/Fe3O4–Eg-based hybrid nanofluid). These studies have all confirmed the dramatic modification achieved in heat and momentum characteristics with the deployment of magnetic and ferromagnetic nanoparticles. However, attention was confined to generally Fe_3O_4 magnetic nanoparticles in these studies. With the progress in nanotechnology, alternative magnetic nanoparticles have emerged such as Mn-Zn ferrite and Cobalt ferromagnetic nanoparticles, which provide a new dimension in functionality owing to their superior magnetic, thermal and also optical properties [32-34]. These offer promise in increasingly diverse technologies including sensor surfaces, piezoelectric devices, sterile and anti-bacterial biomedical coatings [35] due to excellent biocompatibility [36, 37]. Some experimental studies of ferromagnetic nanofluids have also revealed that convective heat transfer characteristics of e. g. 10-nm Fe_3O_4 water based ferrofluid in a heated copper tube are strongly improved with greater magnetic field and magnetic nanoparticle volume fraction [38]. Li and Xuan [39] have also experimentally observed the effect of external magnetic field strength and its orientation on heat transfer characteristics of magnetite nanofluid flow around a fine wire, noting that magnetic field gradient exerts a critical role and the Kelvin forced-induced particle migration is primarily responsible for the observed enhancement. Very recently, Sreedevi et al. have observed the effect of magnetic field and thermal radiation on natural convection in a square cavity filled with TiO_2 nanoparticles [40]. Some recent researchers have explored nanofluid flow where some effective nanoparticle and base fluid combinations are discussed with various significant effects on the thermal enhancement [41-43]

Magnetic induction effects become significant when the magnetic Reynolds number in the regime is sufficiently large to permit distortion of the magnetic field lines [44]. In addition to the Lorentzian magnetic body force, a separate equation is required for the magnetization effect (induced magnetic field) since the motion of a conducting fluid will then generate a magnetic field, distinct from the applied magnetic field. Viscous flows with magnetic induction have been studied by a number of investigators and in particular the interaction with heat and mass diffusion phenomena has been studied in detail. Relevant works include Kumari *et al.* [45] who studied magnetic induction in heat transfer over a stretching sheet and Koshiba *et al.* [46] who examined the influence of induced magnetic field on large scale pulsed MHD generator flow. Ghosh *et al.* [47] derived asymptotic solutions for electrically conducting viscous Newtonian convective flow from a plate with induction effects. They observed that induced magnetic field is enhanced near the plate surface with greater free convection (buoyancy) i. e. thermal Grashof parameter, whereas it is suppressed further into the boundary layer. MHD axisymmetric flow computed for third grade fluid with a stretching cylinder by Hayat et al. [48]. In another paper, Hayat et al [49] explored the inclined magnetic field impact on flow of third grade fluid with variable conductivity, heat source/sink and nonlinear thermal radiation. Similar researches have been done on nanofluid with magnetic field effects for the thermal enhancement [50-53]. Bég *et al.* [54] studied the influence of magnetic induction on squeeze film magnetic flow between two approaching disks. They deployed an Adomian decomposition (power series) method to evaluate the influence of squeeze Reynolds number, axial and tangential magnetic force strength parameters and magnetic Reynolds number on radial and tangential velocity and induced magnetic field components. Very recently Bég *et al.* [55] used a homotopy analysis method (HAM) to investigate the effects of rotational body force and magnetic induction in periodic pumping flow of a partially ionized dielectric hydrogen gas in a duct. Magnetized nanofluid and ferromagnetic nanofluid flows with induced magnetic field effects have also received some attention in recent years. Akbar *et al.* [56] derived closed-form solutions for the metachronal propulsion of Cu-water nanofluids in a two-dimensional channel with magnetic induction. Bég *et al.* [57] investigated the thermocapillary magnetized nanofluid convection flow from a non-isothermal coating sheet with magnetic induction effects. They considered silver, copper, aluminium oxide and titanium oxide magnetic nanoparticles, and showed that induced magnetic stream function is enhanced with magnetic body force parameter. They also noted that significant temperature enhancement but strong flow retardation and decrement in induced magnetic stream function gradient accompany an elevation in nanoparticle solid volume fraction. Further studies in the context of smart (functional) materials processing include Mizwan *et al.* [58] (on ferromagnetic nanofluid flow from a stretching cylinder), Akter *et al.* [59] (on radiative heat transfer in magnetic induction nanofluid convection from a moving surface) and Uddin *et al.* [60] (on magnetic nanofluid coating slip flow from a wedge surface doped with gyrotactic micro-organisms). Bég *et al.* [61] used a finite difference procedure to compute the solar magnetic nano-coating flow on a flat substrate with induction effects. They considered a variety of nanoparticles and observed that Silver nanoparticles, in combination with various base fluids (e. g. kerosene, water and ethylene glycol) produce the best thermal enhancement and boost both velocity and induced magnetic field stream function magnitudes. They further noted that an increment in magnetic Prandtl number strongly accentuates the magnetic induction throughout the boundary layer coating domain. These studies have all confirmed the significant modification in heat and momentum behaviour with inclusion of induced magnetic field in mathematical models.

Motivated by manufacturing processes for functional ferromagnetic nanofluids, in the present article, a mathematical model is developed for *steady incompressible magnetohydrodynamic (MHD) boundary layer stagnation point flow and heat transfer in a nano-ferrofluid along a* *linearly moving stretching sheet with uniform magnetic induction*. The nano-ferrofluid comprises an aqueous base fluid doped with a variety of ferromagnetic nanoparticles i. e. magnetite (Fe_3O_4), cobalt (Co) ferrite and Manganese-Zinc (Mn-Zn) ferrite. Previous studies have considered *stagnation flow* of *non-magnetic nanofluid*s comprising carbon nanotubes [62, 63] and *not ferromagnetic nanofluids*. This is the *novelty* of the present investigation which also included induced magnetic field effects. A modified Maxwell nanoparticle model is deployed. The partial differential conservation equations for mass, momentum, magnetic field continuity (induction) and energy with appropriate wall and free stream boundary conditions, are transformed into a dimensionless nonlinear ordinary differential boundary value problem and solved numerically using the robust bvp4c function in MATLAB (4th order optimized Runge-Kutta quadrature) [65]. Dual solutions for the upper branch and lower branch which are separated by a critical point are identified. Validation of solutions with previous studies is also included. A detailed parametric study is conducted to elucidate the impact of Prandtl number (Pr), nanoparticle volume fraction parameter (φ), reciprocal of magnetic Prandtl number (λ), magnetic parameter (β) and stretching rate ratio parameter (A) on velocity, temperature, induced magnetic field function, skin-friction coefficient and the local Nusselt number. The present problem has thus far not been addressed in the scientific literature and provides a more comprehensive examination of ferromagnetic nanofluid transport phenomena in stagnation flow materials processing coating operations.

2. MATHEMATICAL MODEL FOR FERRO-NANOFLUID STAGNATION FLOW

Consider the two-dimensional, steady, incompressible flow of electrically conducting water- based nano-ferro-fluid at the stagnation point on a stretching moving surface. A Cartesian coordinate system is adopted such that the $x-$ axis is aligned with the horizontal stretching surface (wall) and $y-$ axis is normal to the wall, as shown in **Fig 1**. The base fluid contains one of three different types of ferromagnetic nanoparticles: magnetite (Fe_3O_4), Mn-Zn ferrite and cobalt ferrite ($CoFe_2O_4$). The stretching sheet is isothermal i. e. sustained at uniform temperature T_w and T_∞ corresponds to the ambient fluid temperature (in the free stream). The sheet stretches with a linear velocity $U_w = cx$. $U_e = ax$ corresponds to the free stream velocity far from the plate Here a and c are the positive constants.

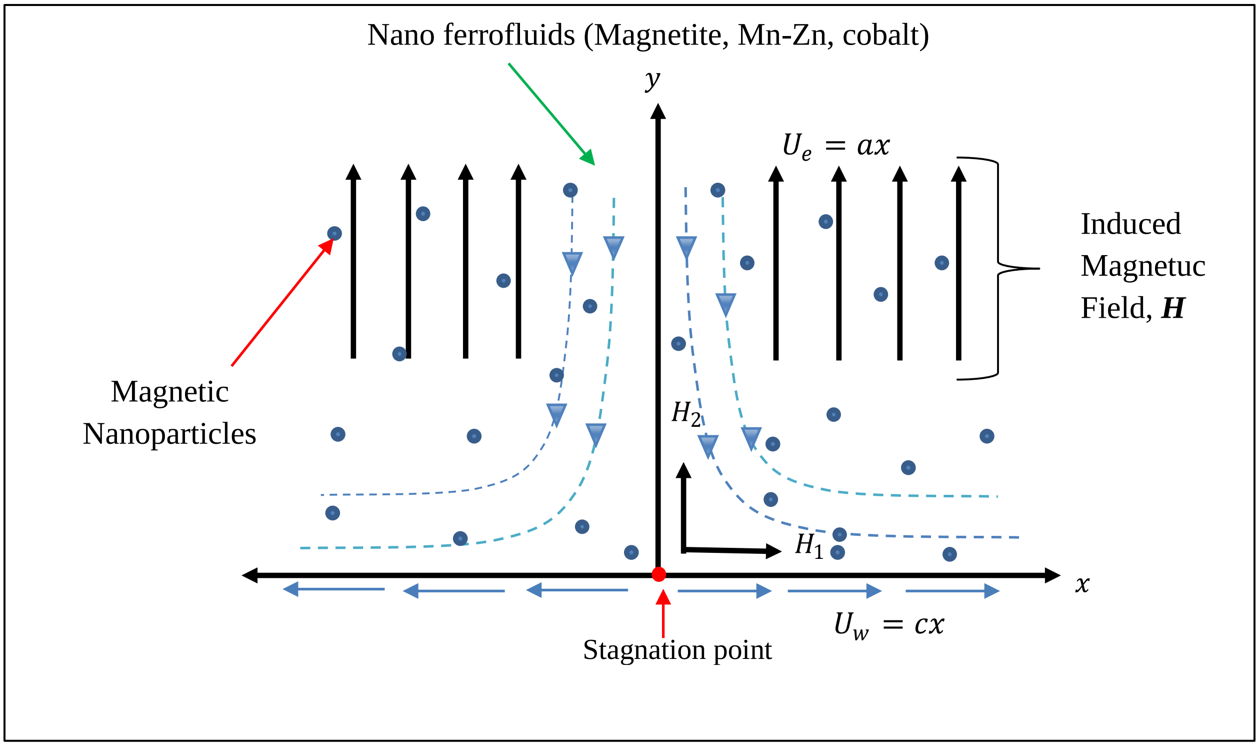

Fig 1: Schematic diagram of stagnation flow of nano-ferrofluid from a stretching sheet

Additionally, it is assumed that $\boldsymbol{H}$ is the induced magnetic field vector with free stream magnetic field component, $H_e = H_0 x$ in which H_0 is the upstream uniform magnetic field at infinity. In addition, the parallel and normal components of induced magnetic field $\boldsymbol{H}$ are denoted H_1 and H_2, respectively. At the surface, the normal component H_2 vanishes whereas the parallel component H_1 becomes H_0. Hall current and ion slip effects are neglected. Under these assumptions, the boundary layer equations governing the stagnation point flow and heat transfer of ferro-nanofluid can be written by amalgamating previous models [24, 26, 30, 66, 67] as:

$$\frac{\partial \bar{u}}{\partial \bar{x}} + \frac{\partial \bar{v}}{\partial \bar{y}} = 0 \qquad (1)$$

$$\frac{\partial \overline{H_1}}{\partial \bar{x}} + \frac{\partial \overline{H_2}}{\partial \bar{y}} = 0 \qquad (2)$$

$$\bar{u}\frac{\partial \bar{u}}{\partial \bar{x}} + \bar{v}\frac{\partial \bar{u}}{\partial \bar{y}} = \frac{\mu}{4\pi\rho_f}\left(\overline{H_1}\frac{\partial \overline{H_1}}{\partial \bar{x}} + \overline{H_2}\frac{\partial \overline{H_1}}{\partial \bar{y}}\right) + \left(\overline{U_e}\frac{\partial \overline{U_e}}{\partial \bar{x}} - \frac{\mu \overline{H_e}}{4\pi\rho_f}\frac{\partial \overline{H_e}}{\partial \bar{x}}\right) + \left(\frac{\mu_{nf}}{\rho_{nf}}\right)\frac{\partial^2 \bar{u}}{\partial \bar{y}^2}$$
$$+ \qquad (3)$$

$$\bar{u}\frac{\partial \overline{H_1}}{\partial \bar{x}}+\bar{v}\frac{\partial \overline{H_1}}{\partial \bar{y}}-\left(\overline{H_1}\frac{\partial \bar{u}}{\partial \bar{x}}+H_2\frac{\partial \bar{u}}{\partial \bar{y}}\right)=\mu_e\frac{\partial^2 \overline{H_1}}{\partial \bar{y}^2} \tag{4}$$

$$\left(\rho C_p\right)_{nf}(\bar{u}\frac{\partial T}{\partial \bar{x}}+\bar{v}\frac{\partial T}{\partial \bar{y}})=k_{nf}\ \frac{\partial^2 T}{\partial \bar{y}^2} \tag{5}$$

Subject to wall and freestream boundary conditions:

$$\bar{u}=\overline{U_w}=c\bar{x},\ \ \bar{v}=0,\ \ T=T_\infty,\ \ \frac{\partial \overline{H_1}}{\partial y}=\overline{H_2}=0\ \ \text{ at }\ y=0$$

$$\bar{u}\to \overline{U_e}=a\bar{x},\ \ T\to T_\infty,\ \ \overline{H}_1=\overline{H}_e(x)\to \overline{H}_0\bar{x}\qquad \text{as }\ y\to\infty \tag{6}$$

The effective properties of ferro-nanofluids are computed using the following relations based on the Xue-Maxwell [64] model as follows:

$$\mu_{nf}=\frac{\mu_f}{(1-\varphi)^{2.5}},\quad \rho_{nf}=(1-\varphi)\rho_f+\varphi\rho_s,$$

$$(c_p)_{nf}=(1-\varphi)(c_p)_f+\varphi(c_p)_s$$

$$\frac{k_{nf}}{k_f}=\frac{(1-\varphi)+2\varphi\frac{k_s}{k_s-k_f}\ln\left[\frac{k_s+k_f}{2k_f}\right]}{(1-\varphi)+2\varphi\frac{k_f}{k_s+k_f}\ln\left[\frac{k_s+k_f}{2k_f}\right]} \tag{7}$$

In Eqns. (1)-(7), $u,\ v,\ H_1$ and H_2 denote the velocity and magnetic components along the $x-$ and $y-$ directions respectively, T denotes the fluid temperature, $\rho_{nf},\ \mu_{nf}$ denote the density, dynamic viscosity of nanofluid respectively. φ is the particle volume fraction parameter, ρ_f and ρ_s are density of fluid and nanoparticles, $(c_p)_{nf}$, $(c_p)_f$, $(c_p)_s$ are specific heats of nanofluid, base fluid and the nanoparticles, respectively, k_{nf}, k_f, k_s are thermal conductivities of nanofluid, base fluid and nanoparticles, respectively. The term $\frac{\kappa_{nf}}{\kappa_f}$ is based on Maxwell theory and Xue's model [64] which accounts for rotational elliptical nanotubes also. The thermophysical properties for water base fluid and different ferromagnetic nanoparticles are listed in **Table 1**.

Physical Properties	Base fluid	Magnetic nanoparticles		
	Water	**Magnetite Ferrite**	**Cobalt Ferrite**	**Mn-Zn Ferrite**
ρ (kg/m^3)	997.1	5180	4907	4900
C_p (J/kg-K)	4179	670	700	800
k (W/m-K)	0.613	9.7	3.7	5.0

Table 1: Aqueous base fluid and ferromagnetic nanoparticle properties

To achieve non-dimensionalisation of the primitive boundary value problem defined by Eqns. (1)-(6), the following non-dimensional scaling variables are invoked:

$$x = \frac{\bar{x}}{\sqrt{\frac{\nu_f}{c}}}\ , \quad y = \frac{\bar{y}}{\sqrt{\frac{\nu_f}{c}}}\ , \quad u = \frac{\bar{u}}{\sqrt{c\nu_f}}\ , \quad v = \frac{\bar{v}}{\sqrt{c\nu_f}}\ , \quad \theta = \frac{T - T_\infty}{T_w - T_\infty}$$

$$H_1 = \frac{\bar{H}_1}{H_0\sqrt{\frac{\nu_f}{c}}}\ , \quad H_2 = \frac{\bar{H}_2}{H_0\sqrt{\frac{\nu_f}{c}}}\ , \tag{8}$$

Eqns. (1) to (5) then emerge in the following non-dimensional form:

$$\frac{\partial u}{\partial x} + \frac{\partial v}{\partial y} = 0 \tag{9}$$

$$\frac{\partial H_1}{\partial x} + \frac{\partial H_2}{\partial y} = 0 \tag{10}$$

$$\left(1 - \varphi + \varphi\frac{\rho_s}{\rho_f}\right)\left(u\,\frac{\partial u}{\partial x} + v\frac{\partial u}{\partial y}\right) =$$

$$\left(1 - \varphi + \varphi\frac{\rho_s}{\rho_f}\right)\left[\frac{\mu}{4\pi\rho_f}\frac{{H_0}^2}{c^2}\left(H_1\frac{\partial H_1}{\partial x} + H_2\frac{\partial H_1}{\partial y} - x\right) + \frac{a^2}{c^2}x\right] + \frac{1}{(1-\varphi)^{2.5}}\frac{\partial^2 u}{\partial y^2} \tag{11}$$

$$hvc\ \ u\frac{\partial H_1}{\partial x}+\ v\frac{\partial H_1}{\partial y}-\ H_1\frac{\partial u}{\partial x}-H_2\frac{\partial u}{\partial y}=\ \frac{\mu_e}{\nu_f}\quad\frac{\partial^2 H_1}{\partial y^2} \tag{12}$$

$$u\frac{\partial\theta}{\partial x}+v\frac{\partial\theta}{\partial y}=\frac{k_{nf}}{\nu_f\left(\rho C_p\right)_{nf}}\cdot\frac{\partial^2\theta}{\partial y^2} \tag{13}$$

The associated dimensionless boundary conditions (6) are:

$$u=U_w=x,\ \ v=0,\quad \theta=1,\ \ \frac{\partial H_1}{\partial y}=H_2=0\quad \text{at}\qquad y=0$$

$$u\to U_e=\frac{a}{c}x\ ,\ \ \theta=0,\quad H_1\to H_e(x)=x\quad \text{as}\qquad y\to\infty \tag{14}$$

Introducing the hydrodynamic and magnetic stream functions ψ and α :

$$u=\frac{\partial\psi}{\partial y}\quad \text{and}\quad v=-\frac{\partial\psi}{\partial x}$$

$$H_1=\frac{\partial\alpha}{\partial y}\quad \text{and}\quad H_2=-\frac{\partial\alpha}{\partial x} \tag{15}$$

Substitution into Eqns. (9) to (13) leads to automatic satisfaction of Eqns. (9) and (10) and the momentum, energy and magnetic induction Eqns. (11)- (13) assume the forms:

$$\left(1-\varphi+\varphi\frac{\rho_s}{\rho_f}\right)\left(\frac{\partial\psi}{\partial y}\frac{\partial^2\psi}{\partial x\partial y}-\frac{\partial\psi}{\partial x}\frac{\partial^2\psi}{\partial y^2}\right)=\left(1-\varphi+\varphi\frac{\rho_s}{\rho_f}\right)\left[\frac{\mu}{4\pi\rho_f}\frac{{H_0}^2}{c^2}\left(\frac{\partial\alpha}{\partial y}\frac{\partial^2\alpha}{\partial x\partial y}-\frac{\partial\alpha}{\partial x}\frac{\partial^2\alpha}{\partial y^2}-x\right)+\frac{a^2}{c^2}x\right]+\frac{1}{(1-\varphi)^{2.5}}\ \frac{\partial^3\psi}{\partial y^3} \tag{16}$$

$$\frac{\partial\psi}{\partial y}\frac{\partial^2\alpha}{\partial x\partial y}-\frac{\partial\psi}{\partial x}\frac{\partial^2\psi}{\partial y^2}-\frac{\partial\alpha}{\partial y}\frac{\partial^2\psi}{\partial x\partial y}+\frac{\partial\alpha}{\partial x}\frac{\partial^2\psi}{\partial y^2}=\frac{\mu_e}{\nu_f}\quad\frac{\partial^3\alpha}{\partial y^3} \tag{17}$$

$$\left(1-\varphi+\varphi\frac{(\rho C_p)_s}{(\rho C_p)_f}\right)\left(\frac{\partial\psi}{\partial y}\frac{\partial\theta}{\partial x}-\frac{\partial\psi}{\partial x}\frac{\partial\theta}{\partial y}\right)=\frac{k_{nf}}{k_f}\cdot\frac{k_f}{\nu_f\left(\rho C_p\right)_{nf}}\frac{\partial^2\theta}{\partial y^2} \tag{18}$$

With corresponding boundary conditions:

$$\frac{\partial\psi}{\partial y}=x\ ,\ \ -\frac{\partial\psi}{\partial x}=0\ ,\ \ \theta=1\ ,\ \ -\frac{\partial\alpha}{\partial x}=0\ ,\ \ \frac{\partial\alpha}{\partial y}=0\ \ \text{at}\quad y=0$$

$$\frac{\partial\psi}{\partial y} = \frac{a}{c}x\ ,\ \theta = 0\ ,\ \frac{\partial\alpha}{\partial y} = x \quad \text{as} \quad y \to \infty \tag{19}$$

Implementing the simplified form of Lie group algebra transformations namely, the scaling group of G-transformations (see- Ibrahim *et al*. [68]), Mukhopadhyay *et al*. [69], Kandasamy and Muhaimin [70], Muhaimin *et al.* [71], Hamad and Pop [72]):

$$\eta = y\ ,\ \psi = x\ f(\eta)\ ,\ \theta = \theta(\eta)\ ,\ \alpha = x\ g(\eta) \tag{20}$$

Substitution into Eqns. (16)-(18) leads to the following system of coupled self-similar nonlinear ordinary differential equations (i. e. momentum, magnetic induction and thermal boundary layer equations):

$$\frac{1}{(1-\varphi)^{2.5}} f''' - \left(1 - \varphi + \varphi\frac{\rho_s}{\rho_f}\right)\left[f'^2 - ff'' - \beta\left(g'^2 - gg'' - 1\right) - A^2\right] = 0 \tag{21}$$

$$\lambda g''' + f.g'' - g.f'' = 0 \tag{22}$$

$$\frac{k_{nf}}{k_f}\ \theta'' + Pr\left(1 - \varphi + \varphi\frac{(\rho C_p)_s}{(\rho C_p)_f}\right) f.\theta' = 0 \tag{23}$$

With corresponding boundary conditions:

$$f'(\eta) = 1\ , f(\eta) = 0\ ,\ g(\eta) = 0\ ,\ g''(\eta) = 0\ ,\ \theta(\eta) = 1 \ \text{ at } \eta = 0$$

$$f'(\eta) = A\ ,\ g'(\eta) = 1\ ,\ \theta(\eta) = 0 \quad \text{as} \quad \eta \to \infty \tag{24}$$

Here, prime indicates differentiation with respect to η. The thermophysical, geometric and magnetic parameters arising in Eqns. (21)-(24) are the Prandtl number (Pr), stretching rate ratio parameter (A), reciprocal of magnetic Prandtl number (λ), magnetic parameter (β) which are defined as follows:

$$\text{Pr} = \frac{(\mu c_p)_f}{k_f}\ ,\ \lambda = \frac{\mu_e}{\nu_f}\ ,\ \beta = \frac{\mu}{4\pi\rho_f}\frac{{H_0}^2}{c^2}\ ,\ A = \frac{a}{c} \tag{25}$$

Here, $A > 0$ corresponds to the situation when the sheet (wall) moves in the *same* direction to the free stream and $A < 0$ when the sheet moves in the *opposite* direction to the free stream, while $A = 0$ is for fixed surface.

The skin friction coefficient C_f and the Nusselt number Nu are defined respectively by:

$$C_f = \frac{\tau_w}{\frac{1}{2}\rho_\infty \bar{u}_\infty{}^2} \, , N_u = \frac{xq_w}{k_f(T_w - T_\infty)} \qquad (26)$$

Here, τ_w and q_w are the wall shear stress and wall heat flux respectively, and take the definitions:

$$\tau_w = \mu_{nf}\left(\frac{\partial \bar{u}}{\partial \bar{y}}\right)_{y=0} \quad , \ q_w = -k_{nf}\left(\frac{\partial T}{\partial \bar{y}}\right)_{y=0} \qquad (27)$$

The desired non-dimensional expressions for skin friction (non-dimensional shear stress) and local Nusselt number (dimensionless temperature gradient at the wall) are as follows:

$$Re_x{}^{-1/2} C_f = \frac{1}{(1-\varphi)^{2.5}} \, f''(0) \, , \quad Re_x{}^{-1/2} \, Nu_x = -\frac{k_{nf}}{k_f} \, \theta'(0) \qquad (28)$$

Here, $Re_x = \frac{u_w \, x}{\nu_f}$ is the local Reynolds number.

3.NUMERICAL SOLUTION WITH MATLAB BVP4C AND VALIDATION

The system of ordinary differential equations (21)-(23) with boundary conditions (24) is strongly nonlinear. An efficient Runge-Kutta quadrature technique is therefore deployed to solve the two-point boundary value problem, namely the 4$^{\text{th}}$ order bvp4c solver in MATLAB [65]. A relationship between the values of the solution is differentiated by the boundary conditions at two or more locations in the interval of integration and the estimation of the error on each sub interval is computed numerically. The bvp4c solver was introduced as an improved technique for solving nonlinear two-point boundary value problems by Kierzenka and Shampine [65] for ordinary differential equations. In bvp4c, the original higher order nonlinear differential equations are changed into a system of first order differential equations and the boundary value problem is converted into an initial value problem by labelling the variables as follows:

$$y_1 = f \, , \quad y_2 = f' \, , \quad y_3 = f'' \, , \quad y_4 = g, y_5 = g' \, , \quad y_6 = g'' \, , \quad y_7 = \theta \, , y_8 = \theta'. \qquad (29)$$

The transformed boundary conditions where ya is the left boundary and yb is the right boundary, are formulated as:

$ya(1) = 0$, $ya(2) - 1 = 0$, $ya(4) = 0$, $ya(6) = 0$, $ya(7) - 1 = 0$ $yb(2) - A = 0$, $yb(5) - 1 = 0, yb(7) = 0.$ (30)

In accordance with the numerical procedure (see Iqbal *et al*. [73]) the system of a first order differential equations can be written as

$$\begin{bmatrix} y_1{}' \\ y_2{}' \\ y_3{}' \\ y_4{}' \\ y_5{}' \\ y_6{}' \\ y_7{}' \\ y_8{}' \end{bmatrix} = \begin{bmatrix} y_2 \\ y_3 \\ (1-\varphi)^{2.5}\left(1-\varphi+\varphi\dfrac{\rho_s}{\rho_f}\right)[y_2{}^2 - y_1y_3 - \beta(y_5{}^2 - y_4y_6 - 1) - A^2] \\ y_5 \\ y_6 \\ \dfrac{1}{\lambda}(y_3y_4 - y_1y_6) \\ y_8 \\ -\dfrac{k_f}{k_{nf}} Pr\left(1-\varphi+\varphi\dfrac{(\rho C_p)_s}{(\rho C_p)_f}\right) y_1y_8 \end{bmatrix}$$

$$\begin{bmatrix} y_1(0) \\ y_2(0) \\ y_3(0) \\ y_4(0) \\ y_5(0) \\ y_6(0) \\ y_7(0) \\ y_8(0) \end{bmatrix} = \begin{bmatrix} 0 \\ 1 \\ z_1 \\ 0 \\ z_2 \\ 0 \\ 1 \\ z_3 \end{bmatrix} \tag{31}$$

Using Newton's method, the appropriate values of initial conditions z_1, z_2 and z_3 are approximated. In order to validate the MATLAB bvp4c computations, we have compared the present results for $A = 0$ i. e. a stationary sheet with those of Ferdows and Alzahrani [28] who used Maple quadrature (trapezoidal method). The comparisons are shown in Fig 2, Fig 3 and Fig 4, for velocity, magnetic stream function and temperature profiles, respectively.

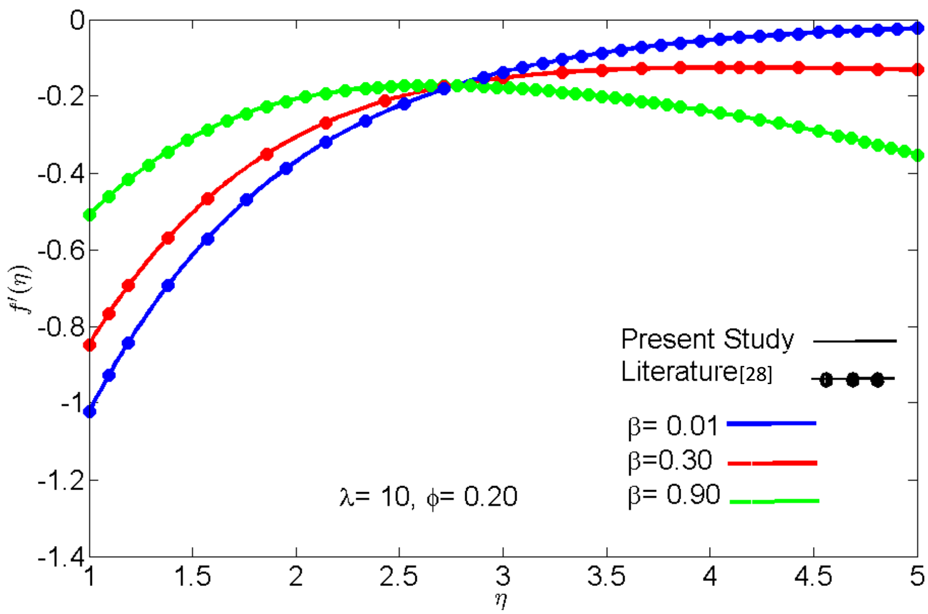

Fig 2: Effects of β on Velocity profile of magnetite particle when $Pr = 6.2$ (Water), $A = 0$, $\varphi = 0.2\,, \lambda = 10$.

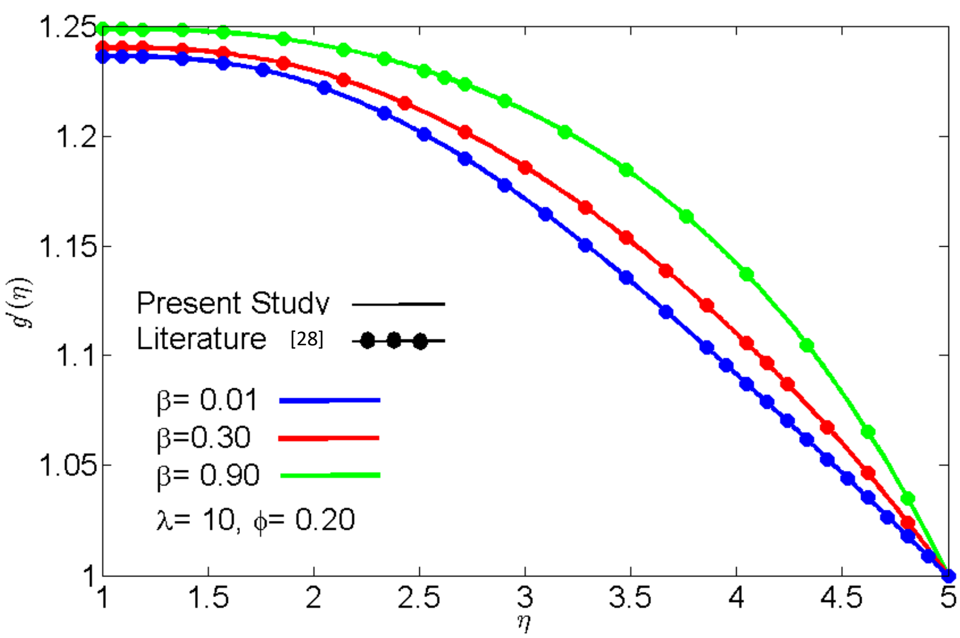

Fig 3: Effects of β on Induced magnetic field profile of magnetite particle when $Pr = 6.2$ (Water), $A = 0$, $\varphi = 0.2\,, \lambda = 10$

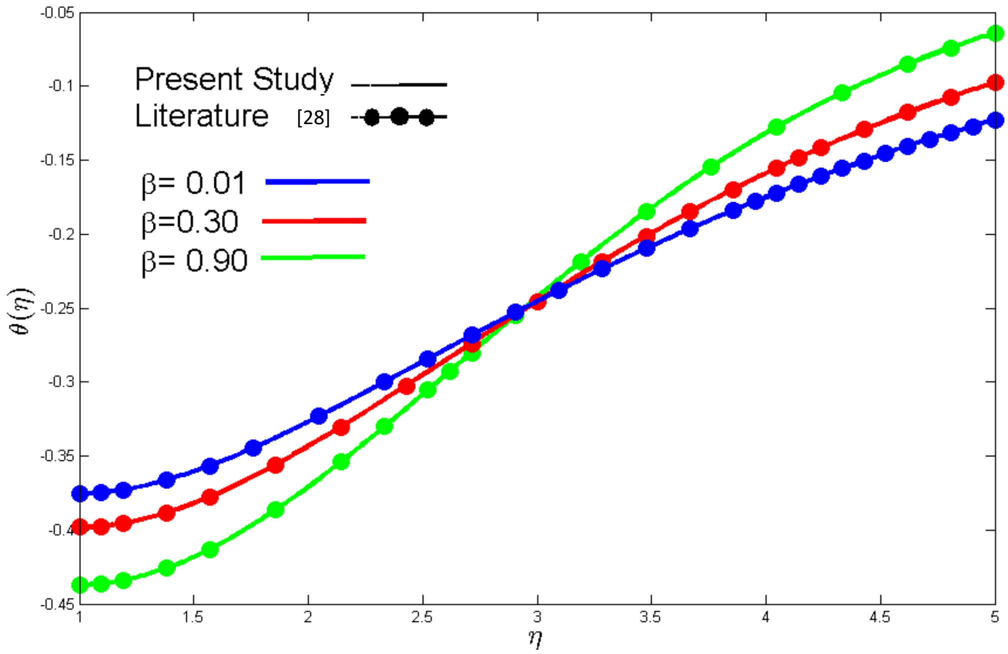

Fig 4: Effects of β on Temperature profile of magnetite particle when $Pr = 6.2$ (Water), $A = 0$, $\varphi = 0.2$, $\lambda = 10$.

Excellent agreement is achieved between the present results and [28] for a variety of magnetic parameter (β) values, and the accuracy of the MATLAB bvp4c method is therefore confirmed.

4.RESULTS AND DISCUSSION

4.1 Skin Friction and Heat Transfer Analysis:

The impact of solid volume fraction parameter (φ) on $f''(0)$ and $-\theta'(0)$ is provided for magnetite, cobalt ferrite and Mn-Zn ferrite nano particles keeping corresponding parameters fixed in **Table 2** and **Table 3**. The dual solutions exist implying the flow separations and reveals that there exist an unrealizable boundary layer approximations. **Table 2** indicates that the rise in solid volume fraction parameter (φ) lowering the skin friction coefficient for all the nanoparticles . This reduction shows higher values for magnetite nanoparticles than cobalt and Mn-Zn ferrite.

φ	Magnetite		Cobalt Ferrite		Mn-Zn Ferrite	
	First Solution	**Second Solution**	**First Solution**	**Second Solution**	**First Solution**	**Second Solution**
0.01	0.80980	-0.028089	0.803220	-0.044278	0.803050	-0.044697
0.02	0.80785	-0.032863	0.801920	-0.047503	0.801767	-0.047881
0.03	0.80537	-0.038963	0.800133	-0.051952	0.799998	-0.052286
0.04	0.80233	-0.046459	0.797842	-0.057689	0.797726	-0.057973
0.05	0.79873	-0.055446	0.795026	-0.064781	0.794931	-0.065012
0.06	0.79453	-0.066019	0.791665	-0.073305	0.791591	-0.073488
0.07	0.78970	-0.092405	0.787736	-0.083367	0.787685	-0.083486
0.08	0.78423	-0.092405	0.783214	-0.095064	0.783188	-0.095121

Table 2: Numerical data of $f''(0)$ for magnetite, cobalt ferrite and Mn-Zn ferrite with representative values of solid volume fraction (φ)

φ	Magnetite		Cobalt Ferrite		Mn-Zn Ferrite	
	First Solution	**Second Solution**	**First Solution**	**Second Solution**	**First Solution**	**Second Solution**
0.01	0.565381	0.280150	0.892040	0.263016	0.773339	0.281338
0.02	0.565102	0.282656	0.892530	0.270946	0.779322	0.286520
0.03	0.571803	0.284802	0.895987	0.277781	0.783277	0.290955
0.04	0.579485	0.286623	0.899412	0.283572	0.789206	0.294697
0.05	0.581149	0.288145	0.905807	0.288406	0.790110	0.297790
0.06	0.589795	0.289393	0.909174	0.292320	0.798991	0.300279
0.07	0.593425	0.290389	0.918514	0.295366	0.799849	0.302199
0.08	0.603039	0.290389	0.949828	0.297591	0.802686	0.303582

Table 3: Numerical data of $-\theta'(0)$ for magnetite, cobalt ferrite and Mn-Zn ferrite with representative values of solid volume fraction (φ)

Table 3 shows the elevation in heat transfer rate with improving solid volume fraction parameter (φ). This is due to the fact that adding the nanoparticles has made the nanofluids more viscous which enhances the resistance between wall and the nanofluid and also therefore enhances the thermal conductivity of the nanofluid.

Skin Friction and Heat Transfer Analysis of Magnetite:

Fig 5 to Fig 10 illustrate the distributions of reduced skin friction, $f''(0)$ and reduced Nusselt number, $-\theta'(0)$, with stretching rate parameter (A) for different ferromagnetic nanoparticles with the base fluid of water. Numerical calculations have been performed for different values of selected parameters which achieve a significant effect. The values of the parameters are prescribed based on appropriate ferromagnetic nanofluid data – see [14], [18], [27], [44], [45] as follows: $A = 1.5$, $\varphi = 0.02$, $Pr = 6.2$ (constant for water-based nano-ferrofluids), $\beta = 0.01$.

Fig 5 and Fig 6 demonstrate the influence of reciprocal magnetic Prandtl number (λ) on the reduced skin friction $f''(0)$ and reduced heat transfer $-\theta'(0)$ for magnetite (Fe_3O_4) nanoparticles. From these figures, it is evident that a dual solution exists for $A_c < A < 0$.
However, there is no solution in the range, $A < A_c$. It is observed that an increase in λ induces the skin friction and the heat transfer to decrease. Magnetic Prandtl number is the ratio of magnetic Reynolds number to ordinary Reynolds number. It expresses also the ratio of viscous diffusion rate (viscosity) to magnetic diffusivity. The reciprocal of this number $\lambda = \frac{\mu_e}{\nu_f}$ therefore quantifies the ratio of magnetic diffusion rate viscous diffusion rate. As this parameter increases, the higher order term, $\lambda g'''$ in the magnetic induction boundary layer Eqn. (22) is boosted. The viscous diffusion rate is reduced and therefore skin friction is suppressed (flow is inhibited), in consistency with Fig. 5. Via the coupling term in the energy Eqn. (23), $+Pr\left(1 - \varphi + \varphi\frac{(\rho C_p)_s}{(\rho C_p)_f}\right) f.\theta'$there will also be a concomitant suppression in heat transfer rate to the wall i. e. reduced Nusselt number will be decreased (Fig. 6). Since Prandtl number is fixed at 6.2, the thermal diffusivity is greater than momentum diffusivity with increasing λ values, and this energizes the boundary layer leading to higher temperature. Less heat is therefore transported to the sheet surface and this manifests in a plummet in reduced Nusselt number at the wall. A modification in reciprocal of magnetic Prandtl number clearly has a substantial impact on momentum and heat transfer characteristics both in the boundary layer regime and at the wall (sheet).

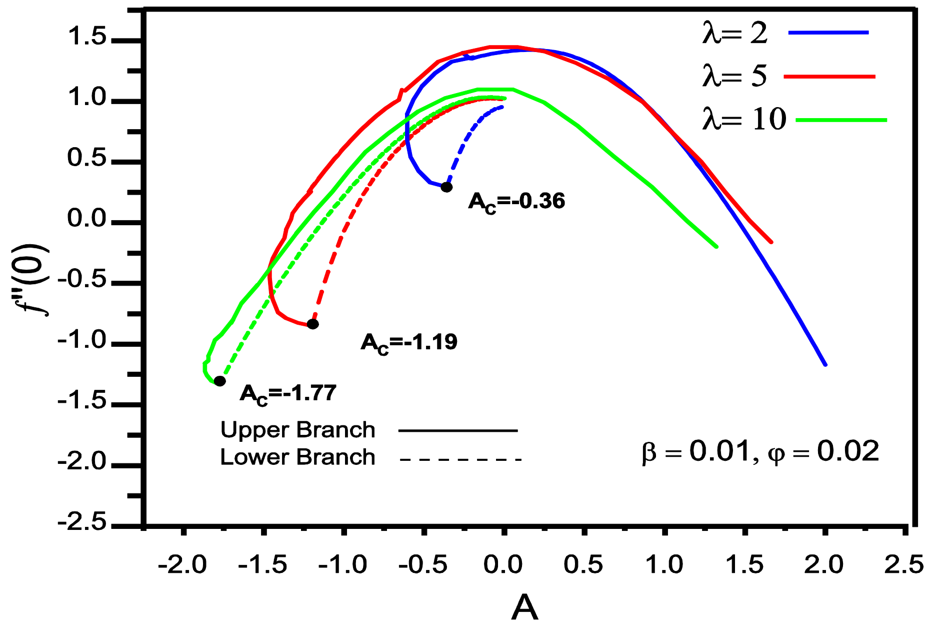

Fig 5: Effects of λ on $f''(0)$ for magnetite nanoparticles when $Pr = 6.2$ (Water), $\beta = 0.01$, $\varphi = 0.02$.

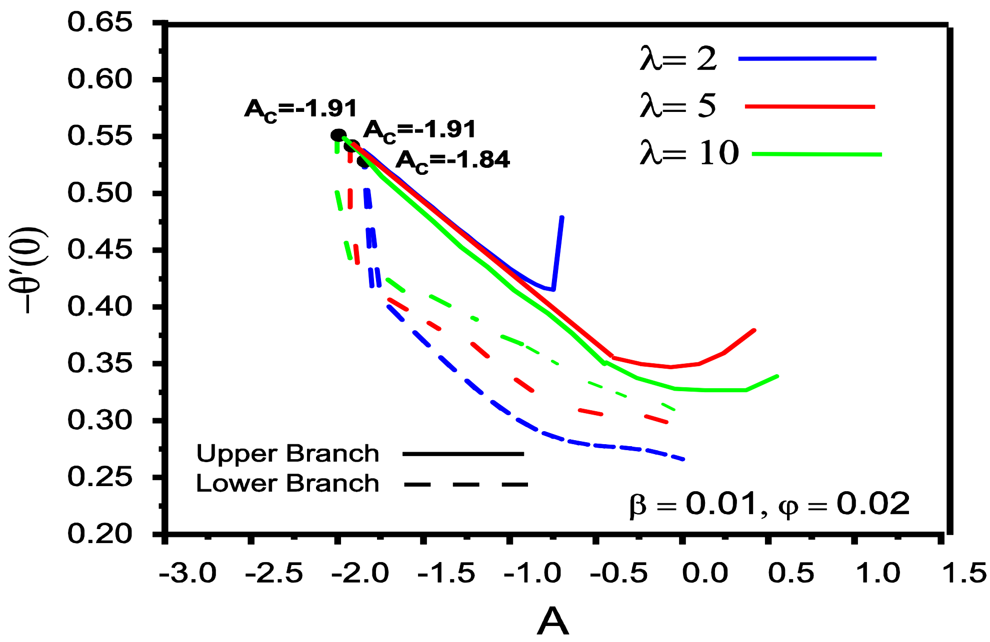

Fig 6: Effects of λ on $-\theta'(0)$ for magnetite nanoparticles when $Pr = 6.2$ (Water), $\beta = 0.01$, $\varphi = 0.02$.

It is also pertinent to note that skin friction is reduced with increasingly negative values of A (i. e. when the sheet moves in the *opposite* direction to the free stream) and also with increasingly positive values of A (when the sheet moves in the *opposite* direction to the free stream) but is maximized consistently when $A = 0$ (fixed surface). Conversely the reduced Nusselt number is elevated with negative A and positive A increment but minimized for fixed surface case ($A = 0$).

Skin Friction and Heat Transfer Analysis of Cobalt Ferrite:

The evolution in reduced skin friction and reduced heat transfer for cobalt ferromagnetic nanoparticles is plotted in **Fig 7 and Fig 8**. In Fig 7, it is seen that when reciprocal magnetic Prandtl number $\lambda = 2$, the critical value for dual solutions becomes $A_c = -0.34$. With an increase in λ from 2 to 5, the range of critical values where the solutions exist is expanded i. e; $A > A_c = -1.23$. With further increment in $\lambda = 10$, the range becomes $A > A_c = -1.93$. It is further revealed that, there will be more resistance between the fluid and the wall causing the solution range to expand which postpones the boundary layer separation. Similarly, Fig 8 displays that the range of critical values which provides the possible existence of dual solution becomes larger with the increase in reciprocal magnetic Prandtl number(λ). In addition, it is evident that with the increase in reciprocal magnetic Prandtl number(λ), the reduced skin friction and reduced heat transfer decrease for the first solution whereas their magnitudes are accentuated for the second solution.

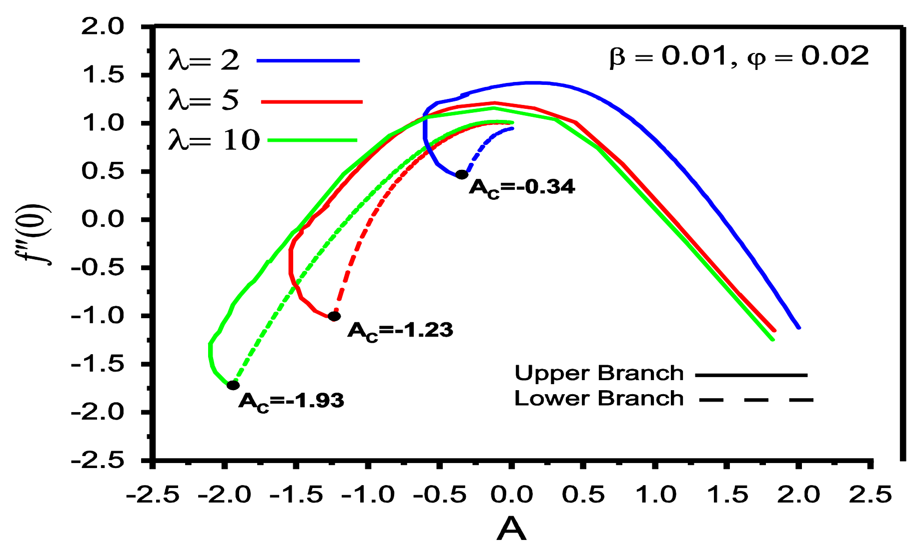

Fig 7: Effects of λ on $f''(0)$ for cobalt nanoparticles when $Pr = 6.2$ (Water), $\beta = 0.01$, $\varphi = 0.02$.

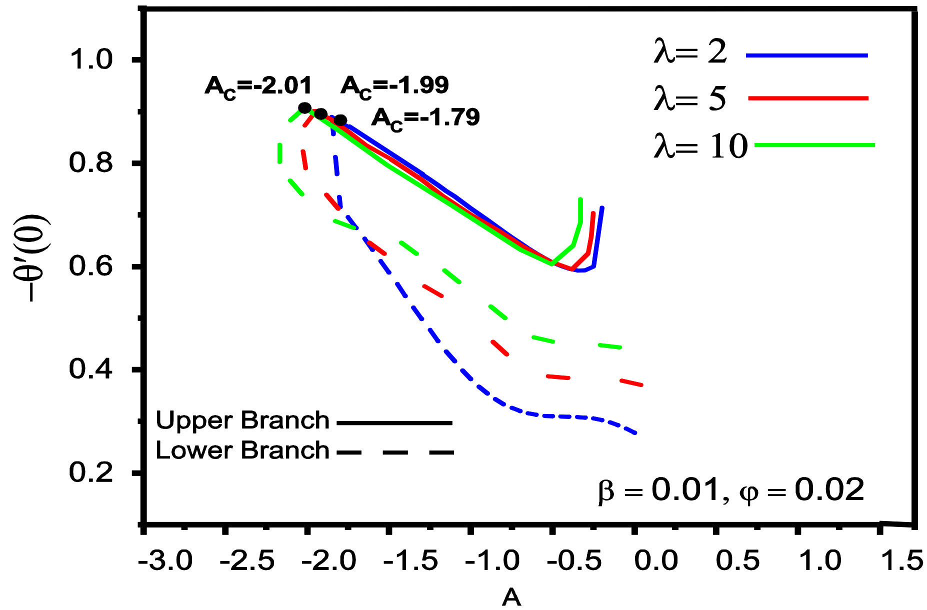

Fig 8: Effects of λ on $-\theta'(0)$ for cobalt nanoparticles when $Pr = 6.2$ (Water), $\beta = 0.01$, $\varphi = 0.02$.

Skin Friction and Heat Transfer Analysis of MN-Zn Ferrite:

Fig 9 and Fig 10 display the influence of reciprocal of magnetic Prandtl number (λ) on reduced skin friction and reduced heat transfer for Mn-Zn ferromagnetic nanoparticles. Fig 9 indicates that for skin friction, the value of reciprocal magnetic Prandtl number $\lambda = 2$ produces a critical value which is equal to -0.925. In other words, solutions exist only when $A > A_c = -0.925$. When reciprocal magnetic Prandtl number increases i. e; $\lambda = 5$, the range of critical value where the possible dual solutions exist becomes $A > A_c = -1.245$. With further increment in reciprocal magnetic Prandtl number to $\lambda = 10$ the range of critical value becomes $A > A_c = -2.004$. Effectively the analysis signifies that the range of existence for dual solutions is increasing with an increment in reciprocal of magnetic Prandtl number (λ). A similar trend is computed for reduced Nusselt number in Fig 10. In addition, it is apparent that when $A < 0$, the reduced skin friction is an *increasing* function whereas for $A > 0$ it is a *decreasing* function. On the other hand, the reduced heat transfer is a decreasing function for $A < 0$ but an increasing function for $A > 0$. With the increasing values of reciprocal magnetic Prandtl number (λ), reduced skin friction and reduced heat transfer are both significantly enhanced. It is further observed that, there will be more resistance between the fluid and the wall causing the solution range to expand which defers the boundary layer separation.

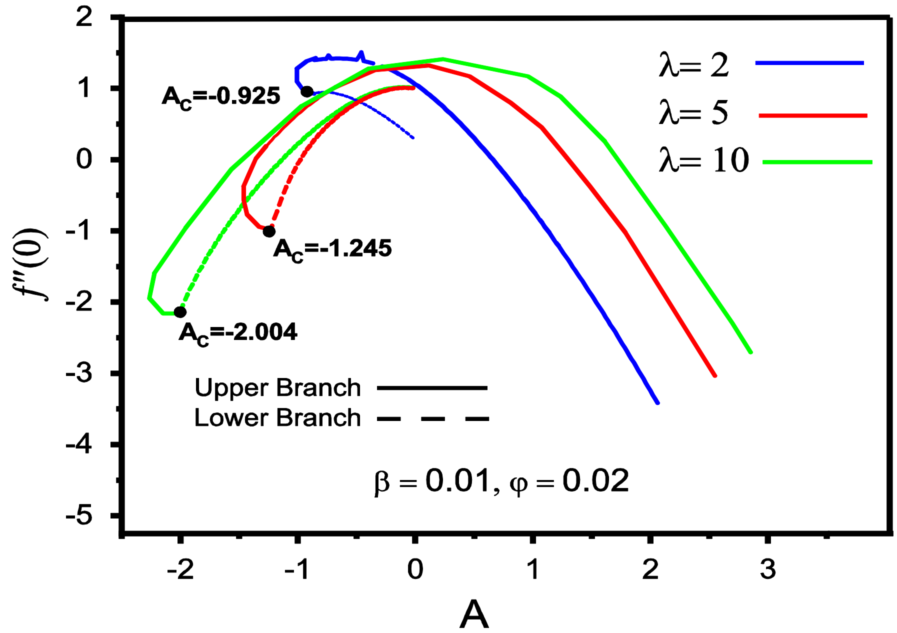

Fig 9: Effects of λ on $-f''(0)$ for cobalt nanoparticles when $Pr = 6.2$ (Water), $\beta = 0.01$, $\varphi = 0.02$.

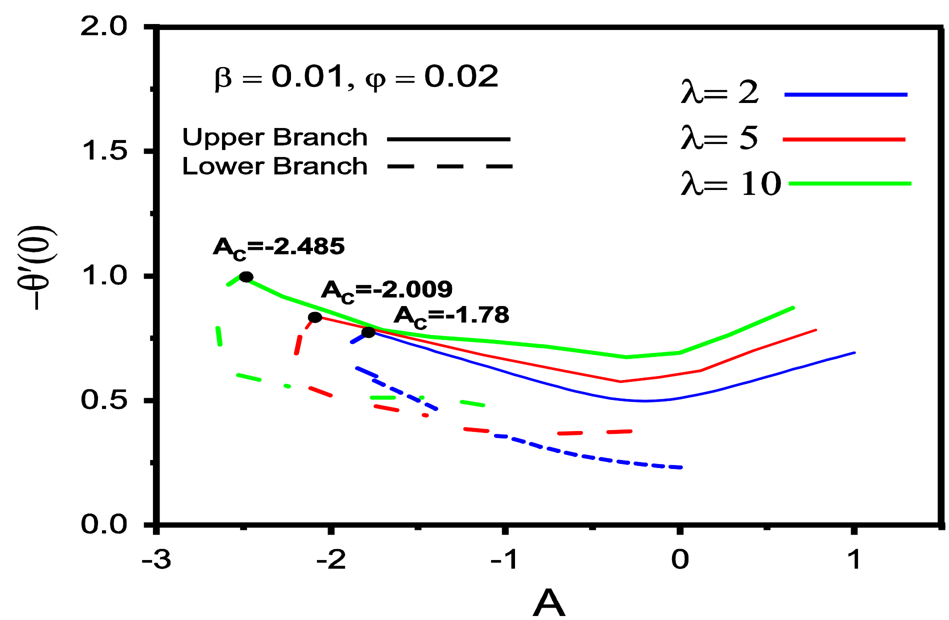

Fig 10: Effects of λ on $-\theta'(0)$ for cobalt nanoparticles when $Pr = 6.2$ (Water), $\beta = 0.01$, $\varphi = 0.02$.

4.2 Flow Analysis*:*

The numerical solutions and dual solution attained graphically are corroborated and verified by fluid velocity $f'(\eta)$, induced magnetic field stream function gradient $g'(\eta)$, and nanoparticles temperature $\theta(\eta)$ profiles versus transverse coordinate (η), all of which converge asymptotically and are displayed in **Figs. 11 to 28**. The prescription of a sufficiently large infinity boundary condition is confirmed by these profiles. It is clearly seen that there are dual solutions in all the plots. The velocity for the first solution always exceeds the second solution whereas the magnetic stream function gradient and temperature for the first solution are consistently exceeded by the second solution. The implication is therefore that the hydrodynamic (momentum) boundary layer thickness of first solution is less than that of the second solution; a similar deduction can be made for the magnetic boundary layer thickness and thermal boundary layer thickness (since these both decrease with a reduction in induced magnetic field and temperature). The *first solution is stable* while the *second solution is unstable* (it has no physical significance). However, for the sake of mathematical rigor, both solutions are included.

The Effect of stretching rate ratio parameter $(\boldsymbol{A})$***:***

The impact of stretching rate ratio parameter (A) on velocity, induced magnetic field and temperature profiles for magnetite particle with $Pr = 6.2$ (Water), $\beta = 0.01$, $\varphi = 0.02$, $\lambda = 10$ are plotted in **Figs. 11 – 13**, respectively. These figures show the existence of dual solutions for the velocity when $A > A_c$ for some representative values of A. In Fig 11 it is noticed that the nature of the solution near the walls and the center is different for both solutions. The velocity is minimum along the centerline and maximum along the wall when $A < 1$. On the contrary, the velocity is maximum along the centerline and minimum along the walls when $A > 1$.

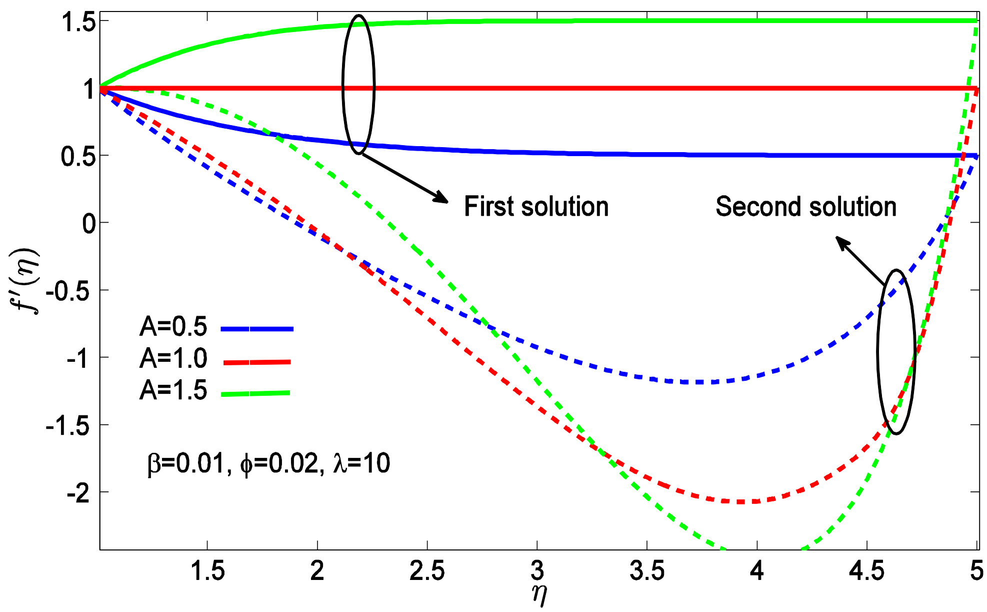

Fig 11: Effects of stretching rate ratio parameter (A) on velocity profile for magnetite nanoparticles when $Pr = 6.2$ (Water), $\beta = 0.01,\ \varphi = 0.02,\ \lambda = 10$.

It is observed that velocity profile is a decreasing function for $A < 1$ and an increasing function for $A > 1$. Velocity profile exhibits an increase with the increase in stretching sheet rate ratio parameter (A) for the first solution. However, the opposite behavior is observed for second solution. It is further observed that the behavior of the velocity near the walls and the center is not same for both solutions. Velocity provides a maximum value at the walls and a minimum value along the center line. It is worth concluding that dual solutions exist in the velocity profiles for accelerated flows when $A > 1$ and decelerated flows when $A < 1$. Fig 12 illustrates that induced magnetic field is an increasing function and it decreases with increasing stretching sheet rate ratio parameter (A) for both solutions. Induced magnetic field is therefore damped with stronger stretching of the sheet in the direction of the free stream. Magnetic boundary layer thickness is therefore suppressed.

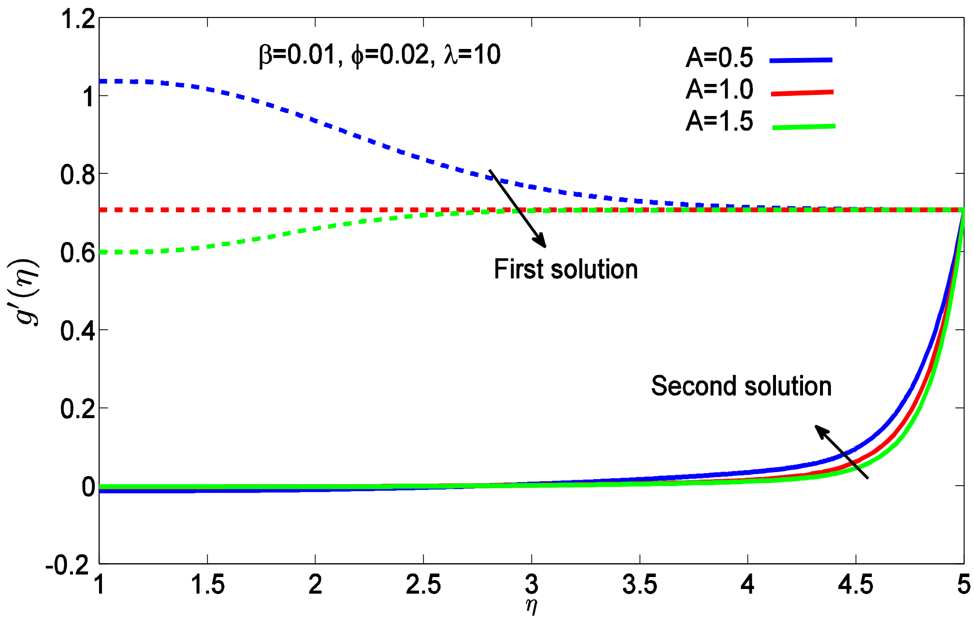

Fig 12: Effects of stretching rate ratio parameter (A) on induced magnetic field profile for magnetite nanoparticles when $Pr = 6.2$ (Water), $\beta = 0.01,\ \varphi = 0.02, \lambda = 10$.

Fig 13 reveals that temperature profile exhibits a decay with increasing stretching rate ratio parameter, $A\ (=\frac{a}{c})$. The thermal boundary layer thickness is therefore strongly depleted with more intense stretching of the sheet in the direction of the free stream. The regime is significantly cooled. So, it can be noted that the accelerating fluid motion reduces the temperature of the nanofluids at the walls. The first solution is *stable* which is physically realizable; however, the second solution is *unstable* with no physical significance. Thermal boundary layer thickness clearly decreases for both solutions.

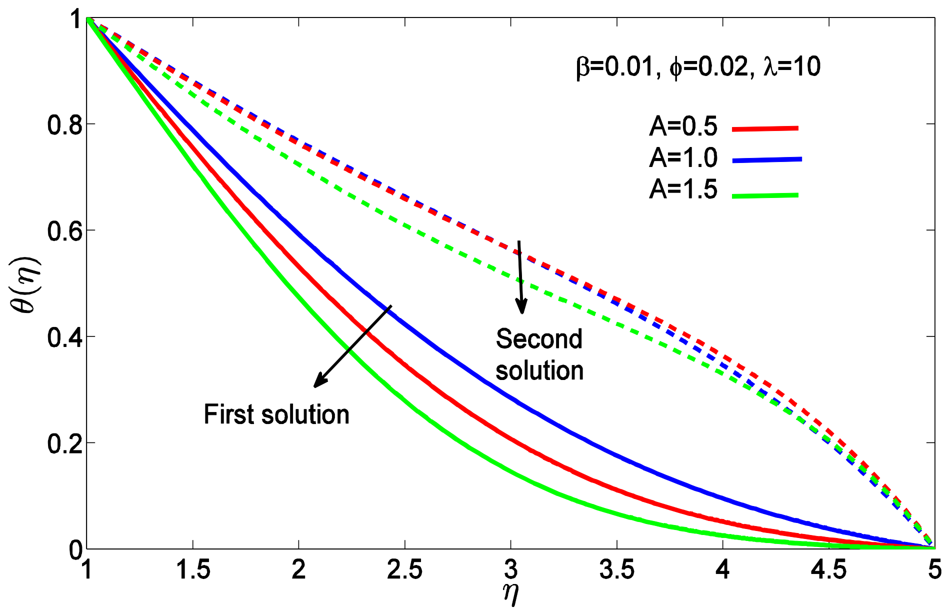

Fig 13: Effects of stretching rate ratio parameter (A) on temperature profile for magnetite nanoparticles when $Pr = 6.2$ (Water), $\beta = 0.01,\ \varphi = 0.02,\ \lambda = 10$.

Figs. 14-16 are plotted to display the variations of velocity, induced magnetic field and temperature profiles for cobalt ferromagnetic nanoparticles within the boundary layer for different values of stretching rate ratio parameter, $A\ (=\frac{a}{c})$. Velocity profile is found to increase with the increasing values of A for the first solution in Fig 14. This is due to the suppression in the drag near the stagnation point which is generated by increasing a in relation to c for a fixed value of $A\ (=\frac{a}{c})$ corresponding to the stretching sheet. This increases the acceleration of the external stream. However, the opposite pattern is computed for the second solution. Momentum boundary layer thickness decreases with increasing in A. In Fig 15, induced magnetic field profile is found to be weakly increased with increment in stretching rate ratio parameter, $A\ (=\frac{a}{c})$ initially, for the *first* solution. However, after a certain point, induced magnetic field stream function gradient retards rapidly. For the *second* solution, there is a marked decay with increasing A. Fig 16 illustrates that with increasing stretching rate ratio parameter, $A\ \left(=\frac{a}{c}\right)$, there is a decay in temperature profile within the boundary layer for *both first and second solutions*. This is associated with the reduced thermal conductivity. So, it can be concluded from figures that cobalt ferrite has the less thermal conductivity than magnetite. It is also apparent that thermal boundary layer thickness for the *first* solution is of lower magnitude relative to the second solution.

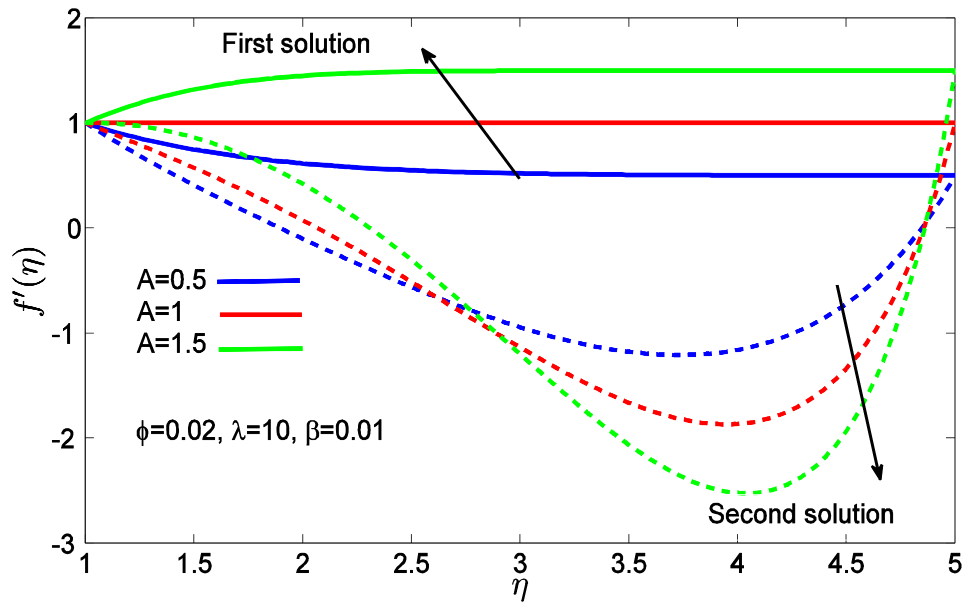

Fig 14: Effects of stretching rate ratio parameter (A) on velocity profile for cobalt nanoparticles when $Pr = 6.2$ (Water), $\beta = 0.01,\ \varphi = 0.02\ ,\ \lambda = 10$.

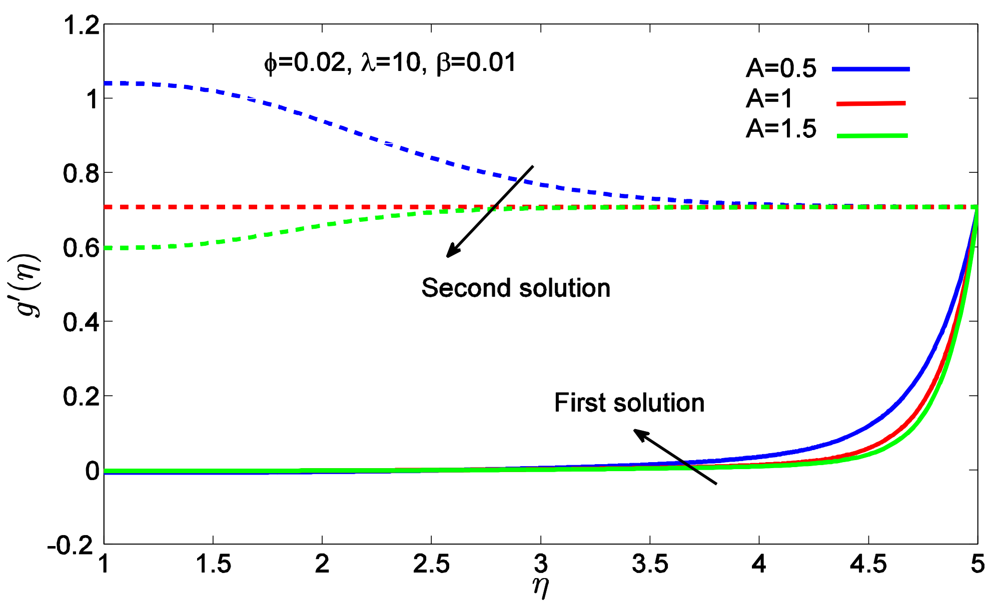

Fig 15: Effects of stretching rate ratio parameter (A) on induced magnetic field profile for cobalt nanoparticles when $Pr = 6.2$ (Water), $\beta = 0.01,\ \varphi = 0.2,\ \lambda = 10$.

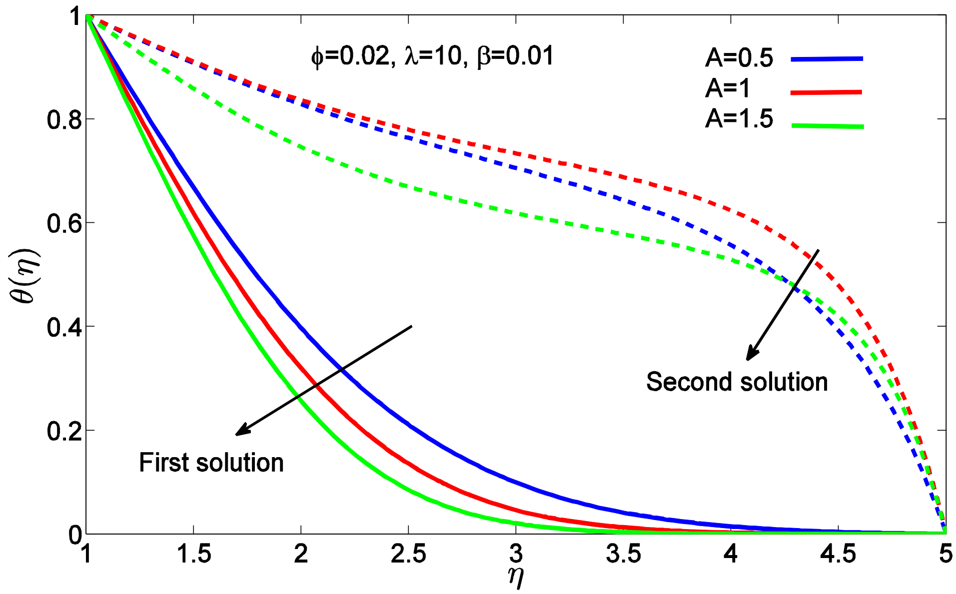

Fig 16: Effects of stretching rate ratio parameter (A) on temperature profile for cobalt nanoparticles when $Pr = 6.2$ (Water), $\beta = 0.01,\ \varphi = 0.02$, $\lambda = 10$.

The effect of stretching rate ratio parameter (A) on velocity, induced magnetic field and temperature profiles for Mn-Zn ferromagnetic nanoparticles with $Pr = 6.2$ (Water), $\beta = 0.01$, $\varphi = 0.02$, $\lambda = 10$ are depicted in **Figs. 17-19**, respectively. Fig 17 demonstrates that the nature of the solution near the walls and the center is different for both solutions. The velocity is a minimum along the centerline and a maximum along the wall (sheet) when $A < 1$. On the contrary, the velocity is maximum along the centerline and minimum along the walls when $A > 1$. The behavior of the velocity profile of Mn-Zn ferromagnetic nanoparticles is similar to that computed earlier for magnetite and cobalt ferromagnetic nanoparticles. A subsequent enhancement appears for the *first* solution with increasing stretching rate ratio parameter (A). On the other hand, the second solution shows a decrement with increasing stretching rate ratio parameter (A). Fig 18 portrays that induced magnetic field stream function gradient is decreased with increment in stretching rate ratio parameter from $A = 0.5$ to $A = 1.5$ for the *first* solution. Magnetic boundary layer thickness therefore diminishes over this range. However, the second solution demonstrates the opposite behavior. Fig. 19 illustrates that temperature decreases significantly with increasing stretching rate ratio parameter (A). The regime is therefore strongly cooled.

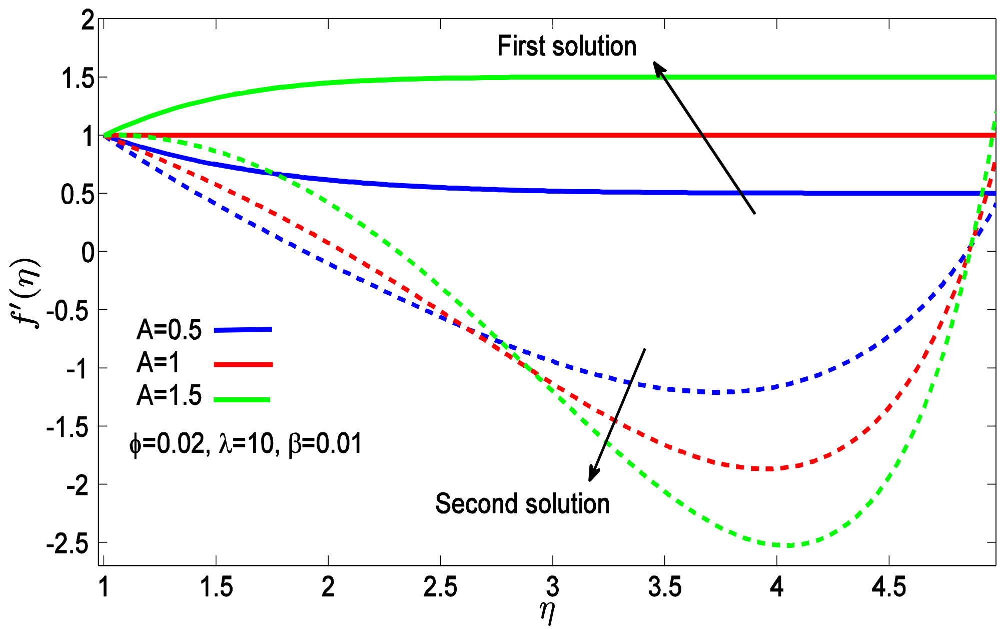

Fig 17: Effects of stretching rate ratio parameter (A) on velocity profile for Mn-Zn nanoparticles when $Pr = 6.2$ (Water), $\beta = 0.01,\ \varphi = 0.02\ , \lambda = 10$.

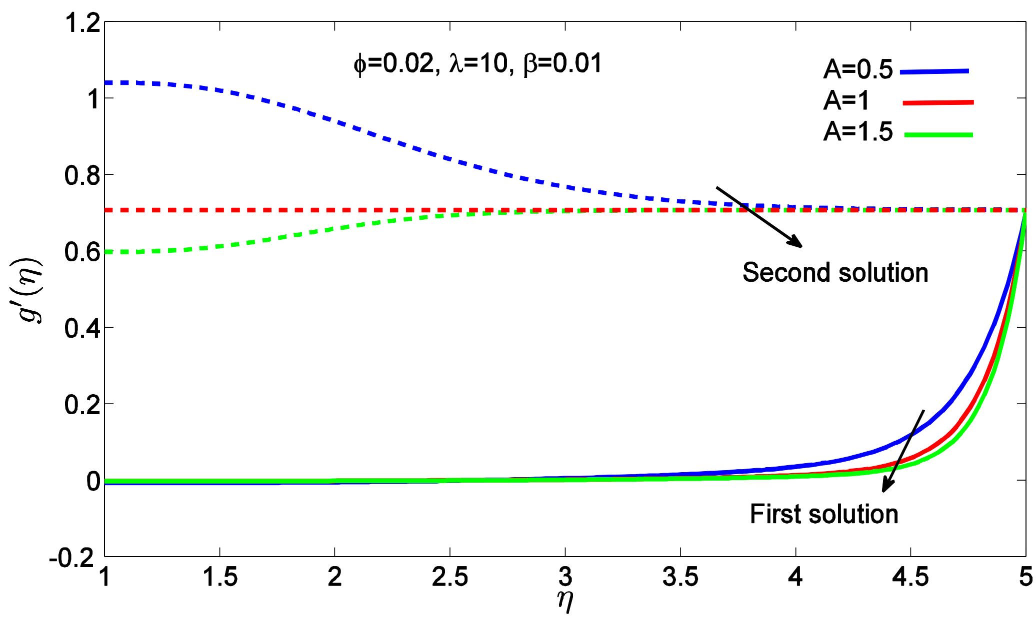

Fig 18: Effects of stretching rate ratio parameter (A) on induced magnetic field profile for Mn-Zn nanoparticles when $Pr = 6.2$ (Water), $= 0.01,\ \varphi = 0.02\ , \lambda = 10$.

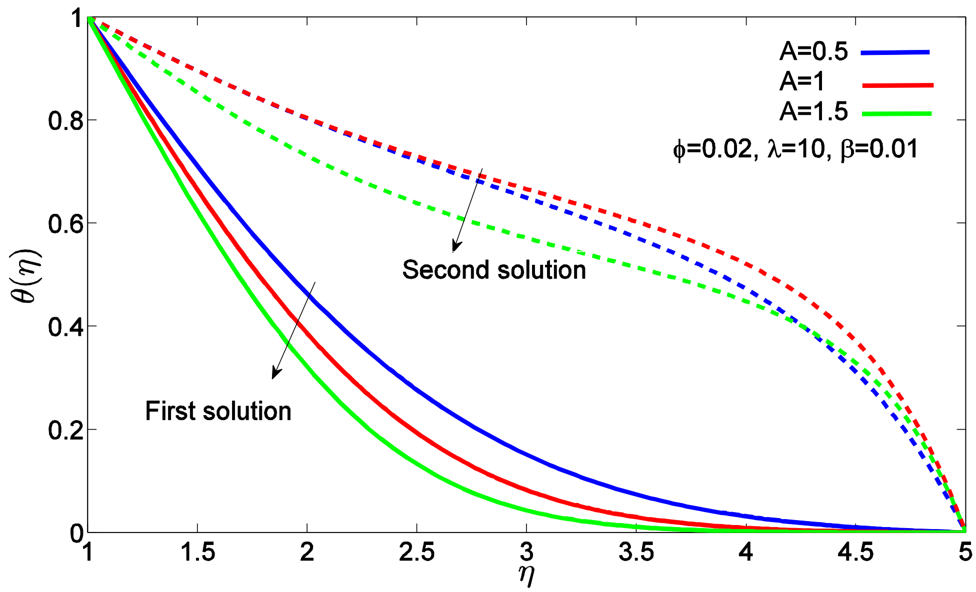

Fig 19: Effects of stretching rate ratio parameter (A) on temperature profile for Mn-Zn nanoparticles when $Pr = 6.2$ (Water), $\beta = 0.01,\ \varphi = 0.02\ , \lambda = 10$.

The effects of magnetic parameter $(\boldsymbol{\beta})$:

Figs. 20, Fig 23 and Fig 26 visualize the influence of magnetic parameter (β) on velocity profiles for respectively, magnetite, cobalt and Mn-Zn nanoparticles with $Pr = 6.2$ (Water), $A = 0.5, \varphi = 0.02, \lambda = 10$ is discussed in respectively. Fig 20 demonstrates that the nature of the solution near the walls and the center is again different for both solutions. A decrement is seen for both solutions with increasing magnetic parameter(β). On the other hand, from the Fig 23 and Fig 26 is may be inferred that completely opposite results for both first and second solution for cobalt and Mn-Zn nanoparticles, respectively are computed i. e. velocity is increased (flow acceleration) with stronger magnetic parameter (β). The magnetization parameter features only in the momentum Eqn. (20) in the terms, $-\beta\left(g'^2 - gg'' - 1\right)$. A significant impact on the shear behaviour of the ferro nanofluid is therefore generated with $\beta = \frac{\mu}{4\pi\rho_f}\frac{{H_0}^2}{c^2}$ (as well as on magnetic induction distribution). The difference in response in velocity is associated with the different electrical conductivity (and magnetic) properties of the different ferromagnetic nanoparticles. For magnetite, velocity is suppressed is suppressed and momentum boundary layer thickness is increased whereas for cobalt and Mn-Zn nanoparticles, velocity is accentuated, and the momentum boundary layer thickness is depleted. The careful selection of ferromagnetic nanoparticle material is therefore critical to achieving desired effects (damping or acceleration) in magnetic functional coatings.

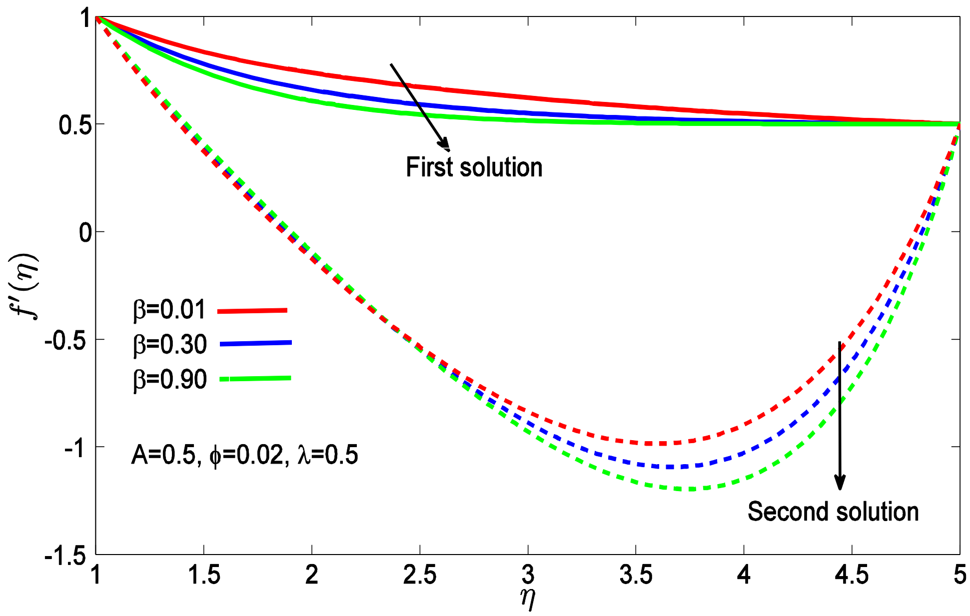

Fig 20: Effects of magnetic particle (β) on velocity profile for magnetite nanoparticles when $Pr = 6.2$ (Water), $A = 0.5,\ \varphi = 0.02, \lambda = 10$.

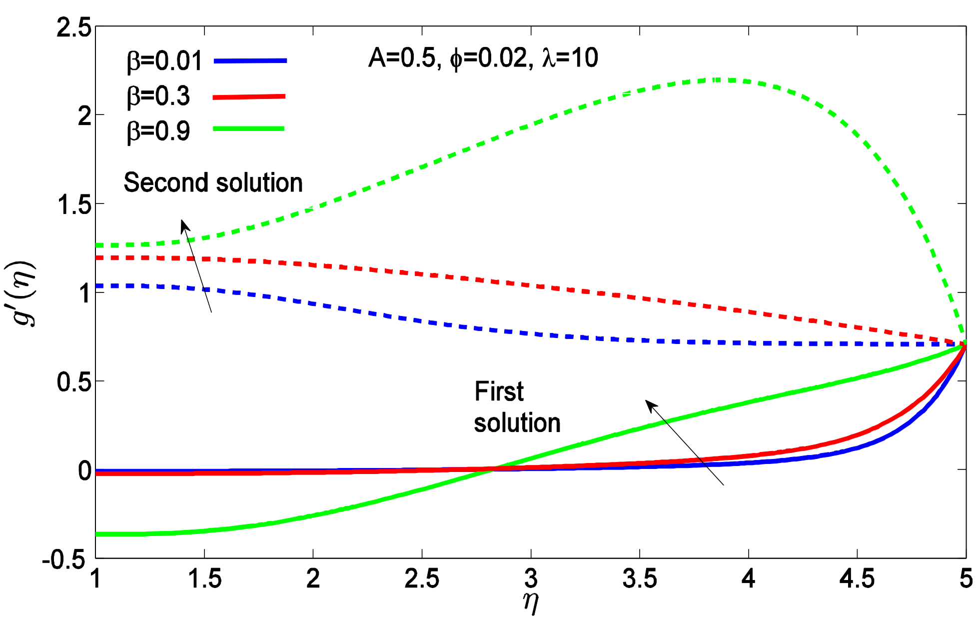

Fig 21: Effects of magnetic particle (β) on induced magnetic field profile for magnetite nanoparticles when $Pr = 6.2$ (Water), $A = 0.5,\ \varphi = 0.02, , \lambda = 10$.

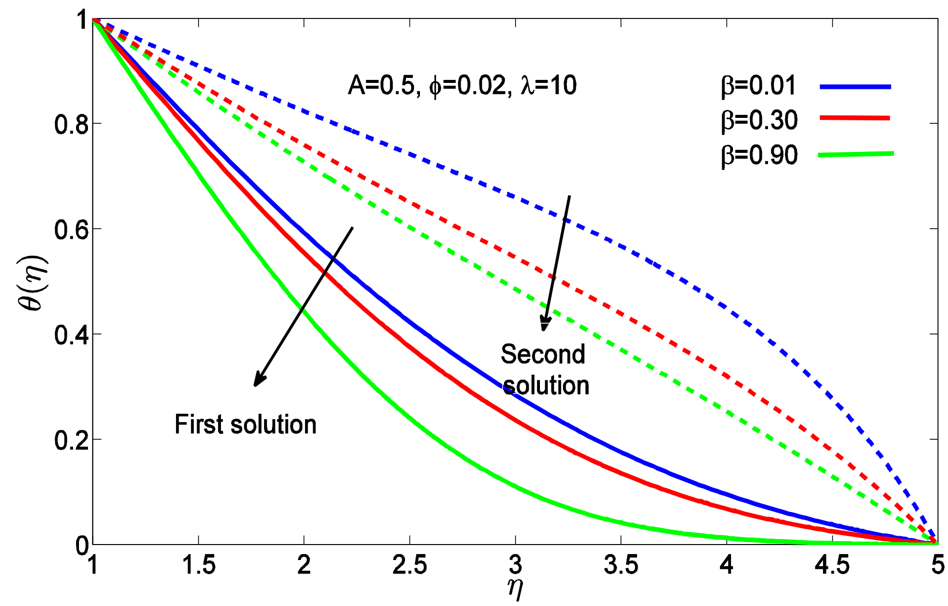

Fig 22: Effects of magnetic particle (β) on temperature profile for magnetite nanoparticles when $Pr = 6.2$ (Water), $A = 0.5,\ \varphi = 0.02, \lambda = 10$.

Fig. 21, Fig 24 and Fig 27 show the induced magnetic field profile for magnetite, cobalt and Mn-Zn nanoparticles respectively with variation in the magnetic parameter (β). It is seen that induced magnetic field profile is substantially increased with increment in value of magnetic parameter , $\beta = 0.01$ to $\beta = 0.90$ for both solutions.

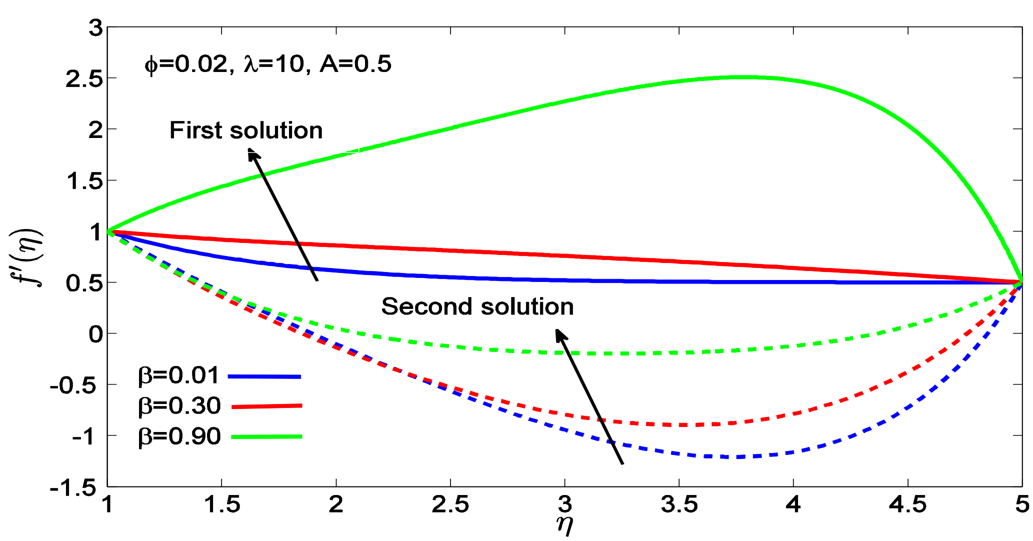

Fig 23: Effects of magnetic parameter (β) on velocity profile for cobalt nanoparticles when $Pr = 6.2$ (Water), $= 0.5,\ \varphi = 0.02, \lambda = 10$.

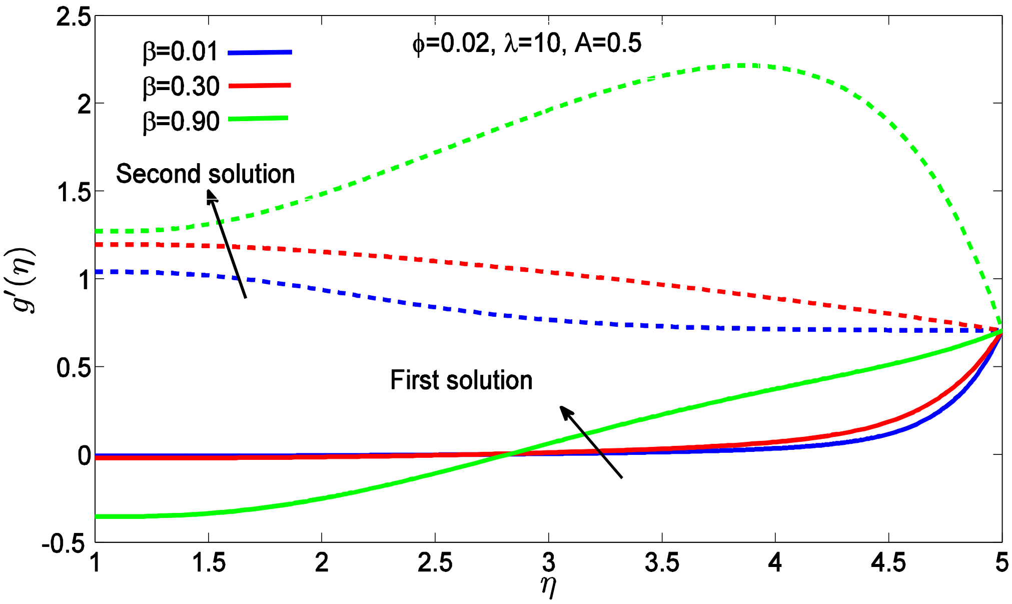

Fig 24: Effects of magnetic parameter (β) on induced magnetic profile of cobalt particle when $Pr = 6.2$ (Water), $A = 0.5,\ \varphi = 0.02,\ \lambda = 10$.

Although β does not feature explicitly in the magnetic induction boundary layer Eqn. (22), the influence is *indirectly experienced via the coupling terms*, $+f.g'' - g.f''$ which intimately link to the momentum Eqn. (21). Strong accentuation in induced magnetic field is produced with amplification in the magnetization parameter and magnetic induction boundary layer thickness is enhanced for both the first and second solutions, albeit only *after* a critical transverse coordinate location for the *former*.

Fig 22, Fig 25 and Fig 28 depict the evolution in temperature for respectively magnetite, cobalt and Mn-Zn nanoparticles with variation in magnetic parameter (β). These figures portray that temperature decreases for increasing magnetic parameter (β) for both first and second solutions. Stronger magnetization therefore cools the boundary layer regime and decreases thermal boundary layer thickness. This effect is the opposite to conventional viscous magnetohydrodynamics (MHD) [44] where increment in an applied magnetic field induces strong heating due to the kinetic energy dissipated via work expended (flow deceleration) in dragging the fluid against the action of the *external* magnetic field.

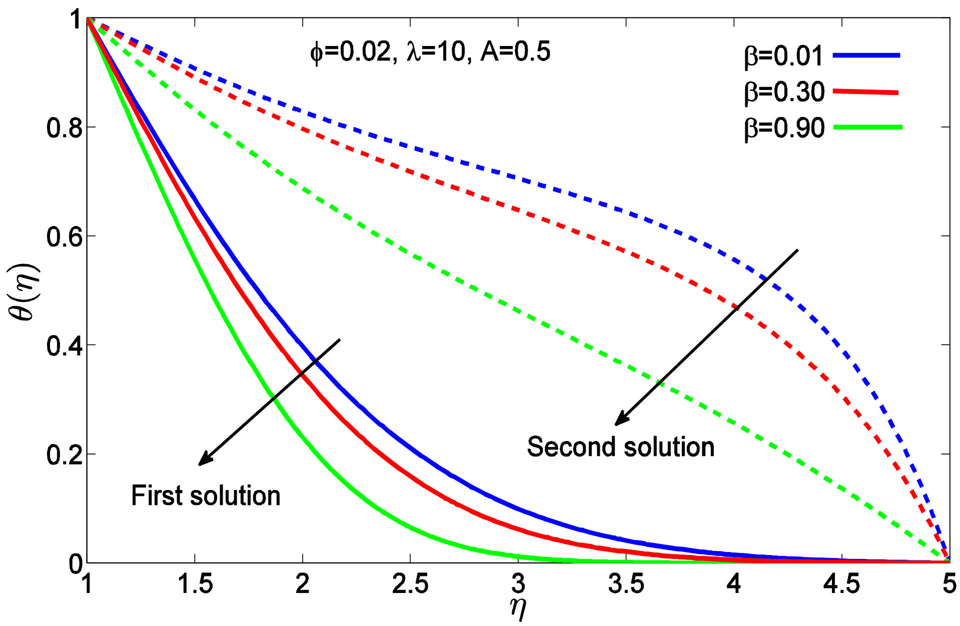

Fig 25: Effects of magnetic parameter (β) on temperature profile for cobalt nanoparticles when $Pr = 6.2$ (Water), $= 0.5,\ \varphi = 0.02, \lambda = 10$.

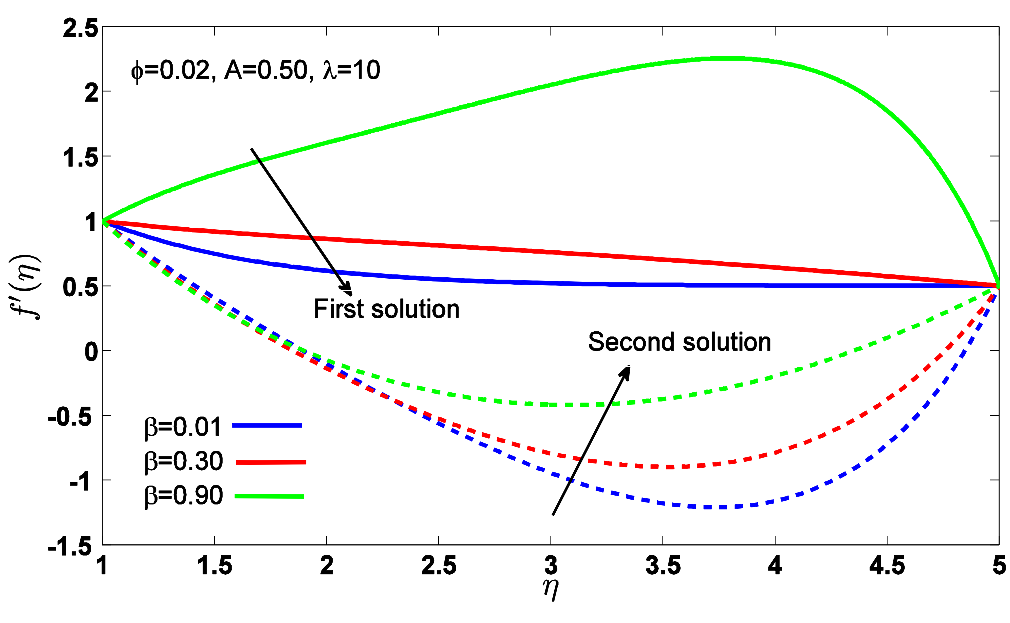

Fig 26: Effects of magnetic parameter (β) on velocity profile for Mn-Zn nanoparticles when $Pr = 6.2$ (Water), $A = 0.5,\ \varphi = 0.02, \lambda = 10$.

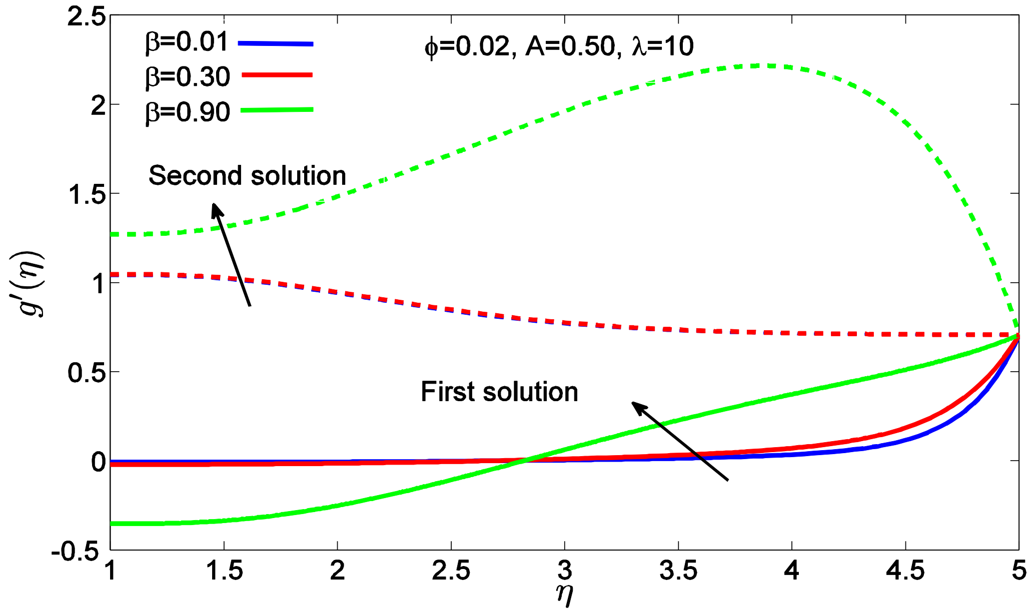

Fig 27: Effects of magnetic parameter (β) on induced magnetic field profile for Mn-Zn nanoparticles when $Pr = 6.2$ (Water), $A = 0.5,\ \varphi = 0.02\ ,\lambda = 10.$

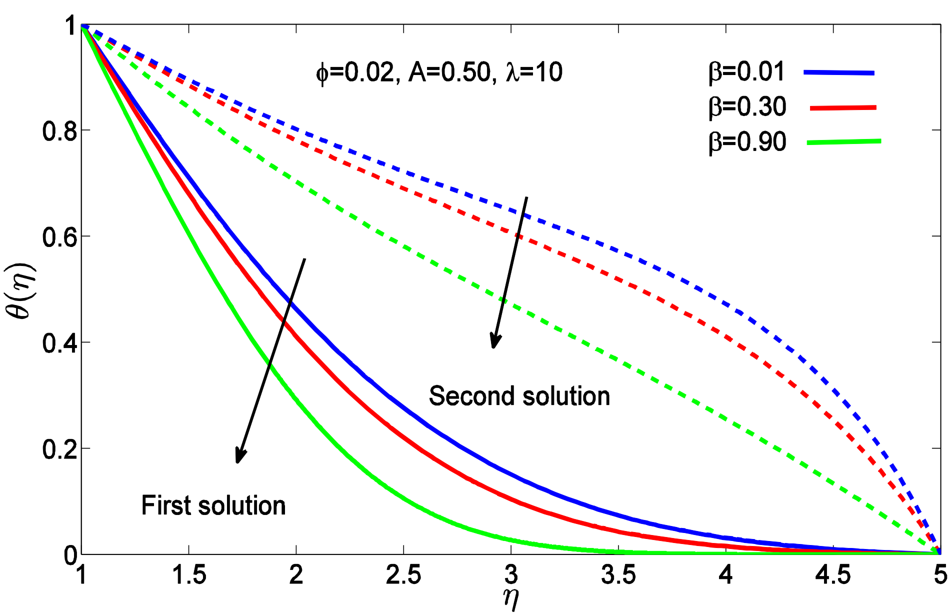

Fig 28: Effects of magnetic parameter (β) on temperature profile for Mn-Zn nanoparticles when $Pr = 6.2$ (Water), $= 0.5,\ \varphi = 0.02\ ,\lambda = 10.$

However, with magnetic induction present, there is an induced magnetic field component along the direction of the wall and the flow is accelerated (not decelerated) with this body force. Therefore, kinetic energy is not dissipated as heat with stronger magnetization effect. Thermal boundary layer thickness is therefore reduced as a result of the cooling generated with greater values of (β). Again, the effect of the magnetization parameter (β) on temperature is due to the coupling terms between the momentum Eqn. (21) and the energy Eqn. (23) as (β) only features in the former and is absent in the latter. The coupling term, $+Pr\left(1-\varphi+\varphi\frac{(\rho C_p)_s}{(\rho C_p)_f}\right) f.\theta'$ in Eqn. (23) is strongly modified by the velocity field which in turn is substantially morphed by the magnetization parameter, via the magnetic induction term, $-\beta\left({g'}^2-gg''-1\right)$. Similar findings have been reported for other ferromagnetic nanoparticles in magnetic induction boundary layer flows in [57], [58] and [66] confirming the validity of the present observations.

5. CONCLUSIONS

In present work, a mathematical model has been developed for the steady magnetohydrodynamic (MHD) boundary layer stagnation point flow of a nano-ferrofluid along a linearly moving stretching sheet, as a simulation of functional magnetic materials processing. The nano-ferrofluid comprises an aqueous base fluid doped with three different ferromagnetic nanoparticles i. e. magnetite (Fe_3O_4), cobalt ($CoFe_2O_4$)o and Manganese-Zinc (Mn-Zn). Magnetic induction is included in the analysis and the Maxwell-Xue nanoscale model is adopted for nanoparticle and base fluid thermophysical properties. A nonlinear dimensionless ordinary differential equation boundary value problem is derived by means of similarity transformations. Numerical solutions have been obtained by employing the robust bvp4c function in MATLAB which features very efficient 4th order optimized Runge-Kutta quadrature. The existence of dual similarity solutions is also included. Solutions for the upper branch and lower branch are shown to be separated by a critical point in terms of the stretching rate ratio parameter. A detailed parametric study of the impact of Prandtl number (Pr), nanoparticle volume fraction parameter (φ), reciprocal of magnetic Prandtl number (λ), magnetic parameter (β) and stretching rate ratio parameter (A) on velocity, temperature, induced magnetic field function, skin-friction coefficient and the local Nusselt number has been conducted. The principal findings of the current simulations may be summarized as follows:

(i)For stretching rate ratio (A) >1, velocity is enhanced whereas induced magnetic field profile as well as temperature profile is reduced. The velocity is a minimum along the centerline and a maximum along the wall (sheet) when $A < 1$. On the contrary, the velocity is maximum along the centerline and minimum along the walls when $A > 1$.

(ii)The behavior of the velocity profile of Mn-Zn ferrite ferromagnetic nanoparticles is similar to that computed for magnetite (Fe_3O_4) and cobalt ferrite ($CoFe_2O_4$) ferromagnetic nanoparticles. A subsequent enhancement appears for the *first* solution with increasing stretching rate ratio parameter (A). On the other hand, the second solution shows a decrement with increasing stretching rate ratio parameter (A).

(iii) Induced magnetic field stream function gradient is decreased with increment in stretching rate ratio parameter from $A = 0.5$ to $A = 1.5$ for the *first* solution. Magnetic boundary layer thickness therefore diminishes over this range. However, the second solution demonstrates the opposite behavior.

(iv)Strong accentuation in induced magnetic field is produced with amplification in the magnetization parameter and magnetic induction boundary layer thickness is enhanced for both the first and second solutions.

(v)Temperatures are decreased with an increase in magnetic parameter (β) i.e. cooling is induced in the regime and thermal boundary layer thicknesses are suppressed.

(vi) Temperature decreases significantly with increasing stretching rate ratio parameter (A). The regime is therefore strongly cooled and thermal boundary layer thickness suppressed for the case where stretching is in the same direction as the freestream (A >0).

(vii)Skin friction and Nusselt number are found to be greater for cobalt nanoparticles when compared to magnetite and Mn-Zn ferromagnetic nanoparticles when there is an increase in reciprocal of the magnetic Prandtl number. At the boundary, the resistance between the wall and fluid is maximized which causes the solution range to expand and this expansion takes place in the range where dual solutions exist.

The MATLAB vbp4c simulations have revealed some interesting characteristics for the stagnation point flow of different ferromagnetic water-based nanofluids of relevance to coating manufacturing processes. However, attention has been confined to *Newtonian* nanofluids. Future investigations may address rheological behaviour of functional ferromagnetic nano-coatings via the Maxwell viscoelastic [74] and tangent hyperbolic shear-thinning [75] models. Efforts in this direction are currently underway and will be reported in the near future.

NOMENCLATURE

$(\bar{x}, \bar{y})$	Cartesian co-ordinate system
$(\bar{u}, \bar{v})(ms^{-1})$	Velocity components along the x and y-direction respectively
$(\bar{H}_1, \bar{H}_2)$	Induced magnetic field components along the x and y-direction respectively
$\bar{U}_w(ms^{-1})$	Velocity of stretching sheet
$\bar{U}_e(ms^{-1})$	Free stream velocity
$\bar{H}_e(Am^{-1})$	Free stream magnetic field
$H_0(Am^{-2})$	Upstream magnetic field at infinity
$T(K)$	Fluid temperature inside the boundary layer
$T_\infty(K)$	Free stream fluid temperature
$T_0(K)$	Ambient temperature
$T_w(K)$	Surface temperature
$q_w(\text{Cal.}\, m^{-2}s^{-1})$	Wall heat flux
φ_w	nano particle volume fraction at the surface
φ_∞	ambient values of nanoparticle volume fraction
$c_p(Jkg^{-1}K^{-1})$	Specific heat at constant pressure
$(c_p)_{nf}(Jkg^{-1}K^{-1})$	Specific heat of nanofluid
$(c_p)_f(Jkg^{-1}K^{-1})$	Specific heat capacity of base fluid
Pr	Prandtl number
Re_x	Local Reynolds number
$f'(\eta)$	Dimensionless velocity
$\theta(\eta)$	Dimensionless temperature
$g'(\eta)$	Dimensionless induced magnetic field

C_f	Local skin friction coefficient
Nu_x	Local Nusselt number
A	Stretching rate ratio parameter

Greek symbols

β	Magnetic parameter
φ	Solid volume fraction parameter
λ	Reciprocal magnetic Prandtl number
$\rho_\infty(kgm^{-3})$	Free stream fluid density
$\rho_{nf}(kgm^{-3})$	Density of the nanofluid
$\rho_s(kgm^{-3})$	Density of nano particle
$\tau_w(Pa)$	Wall shear stress
$\mu(Kgm^{-1}s^{-1})$	Dynamic viscosity of the fluid
$\mu_{nf}(Kgm^{-1}s^{-1})$	Dynamic viscosity of the nanofluid
$\mu_\infty(Kgm^{-1}s^{-1})$	Dynamic viscosity of the fluid in the free stream
$\nu(m^2s^{-1})$	Kinematic viscosity
$\nu_{nf}(m^2s^{-1})$	Kinematic viscosity of the nanofluid
$\nu_\infty(m^2s^{-1})$	Kinematic viscosity in the free stream
$\kappa(Wm^{-1}K^{-1})$	Thermal conductivity of the fluid
$\kappa_{nf}(Wm^{-1}K^{-1})$	Thermal conductivity of the nanofluid
$\kappa_s(Wm^{-1}K^{-1})$	Thermal conductivity of nano particle
$\kappa_\infty(Wm^{-1}K^{-1})$	Thermal conductivity of the fluid in the free stream
α_{nf}	Thermal diffusivity of nanofluid

Conflict of interest: None.

REFERENCES

[1] X. Liu X. *et al.* Reconfigurable ferromagnetic liquid droplets. *Science.* 365:264 (2019).

[2] J. Alam *et al.*, Corrosion-protective performance of nano polyaniline/ferrite dispersed alkyd coatings, *Journal of Coatings Technology and Research*, 5, 123–128 (2008).

[3] Rout TK, Jha G, Singh AK, Bandyopadhyay N, Mohanty, On development of conducting polyaniline coating: a novel approach to superior corrosion resistance. *Surf. Coat. Technol.* 157, 16–24 (2003).

[4] Guilemany JM, Dosta S, Nin J, Miguel JR (2005). Study of the properties of WC-Co nanostructured coatings sprayed by high velocity oxy fuel. *J. Thermal Spray Technol*. 14, 405–413.

[5] S. García-Jimeno and J. Estelrich, Ferrofluid based on polyethylene glycol-coated iron oxide nanoparticles: Characterization and properties, *Colloids and Surfaces A: Physicochemical and Engineering Aspects,* 420, 74-81 (2013).

[6] C.Y. Lee and J.A. Tallmadge, The stagnation point in free coating, *AIChemE J.*, 19 (4), 865-866 (1973).

[7] J.A. Hearley, J.A. Little, and A.J. Sturgeon, The effect of spray parameters on the properties of high velocity oxy-fuel NiAl intermetallic coatings, *Surf. Coat. Technol.*, 123, 210-218 (2000).

[8] Z. Khan, H. Rasheed, Q. Shah, T. Abbas, and M. Ullah, Numerical simulation of double-layer optical fiber coating using Oldroyd 8-constant fluid as a coating material, *Optical Engineering*, 57, no. 7, Article ID 076104 (2018).

[9] O. Anwar Bég, R. Bhargava, S. Sharma, Ali Kadir, Tasveer A. Bég, M. Shamshuddin, Numerical solutions for axisymmetric non-Newtonian stagnation enrobing flow, heat and mass transfer with application to cylindrical pipe coating dynamics, *Computational Thermal Sciences*, 12 (1) 79-97 (2020).

[10] F. Davard, D. Dupuis, Flow Visualization experiments in a blade coating process, *J. Non-Newtonian Fluid Mech.* 93, 17-28 (2000).

[11] K. Hiemenz, Grenzschicht an einem in den gleichformingen Flussigkeits-strom einge-tauchten graden Kreiszylinder, *Dingler's Poly. J*. 326, 321-324 (1911).

[12] Sparrow, EM, Cess, RD. Temperature-dependent heat sources or sinks in a stagnation point flow, *Appl Sci Res, A*, 10: 185-197 (1961).

[13] R.S.R. Gorla, Non-Newtonian fluid at a stagnation point in the presence of transverse magnetic field, *Mech. Res. Comm*., 3, 1-6 (1976).

[14] R. Vajtai (*ed*), *Springer Handbook of Nanomaterials*, Springer-Verlag Berlin Heidelberg (2013).

[15] P. Sreedevi, P. Sudarsana Reddy, Impact of Convective Boundary Condition on Heat and Mass Transfer of Nanofluid Flow Over a Thin Needle Filled with Carbon Nanotubes, *Journal of Nanofluids*, 9 (4), 282-292, (2020)

[16] P. Sreedevi, P. Sudarsana Reddy, Effect of Cattaneo–Christov heat flux on heat and mass transfer characteristics of Maxwell hybrid nanofluid flow over stretching/shrinking sheet, P *Phys. Scr*. 96, 125237, (2021)

[17] M. Ferdows, Tahia Tazin, O. Anwar Bég, Tasveer A. Bég, Dual Solutions in Hiemenz Flow of an Electro-Conductive Viscous Nanofluid Containing Elliptic Single-/Multi-Wall Carbon Nanotubes With Magnetic Induction Effects, *ASME Open J. Eng*., 1, 011040, 2022.

[18] P. Agnihotri and V. N. Lad, Magnetic nanofluid: synthesis and characterization, *Chemical Papers*, 74, 3089–3100 (2020).

[19] F. Fan, Terahertz chiral sensing and magneto-optical enhancement for ferromagnetic nanofluids in the chiral metasurface, *Nanoscale Adv.*, 3, 4790-4798 (2021).

[20] P. Sreedevi, P. Sudarsana Reddy, Entropy generation and heat transfer analysis of alumina and carbon nanotubes based hybrid nanofluid inside a cavity, *Phys. Scr*. 96 085210, (2021).

[21] P. Sudarsana Reddy, P. Sreedevi, Entropy generation and heat transfer analysis of magnetic hybrid nanofluid inside a square cavity with thermal radiation. *Eur. Phys. J. Plus* 136, 39 (2021). https://doi.org/10.1140/epjp/s13360-020-01025-z

[22] P. Sudarsana Reddy, P. Sreedevi, V. Nageswara Reddy, Entropy generation and heat transfer analysis of magnetic nanofluid flow inside a square cavity filled with carbon nanotubes, *Chemical Thermodynamics and Thermal Analysis*, 6, 100045, (2022)

[23] M. Bahiraei, M. Hangi, Investigating the efficacy of magnetic nanofluid as a coolant in double-pipe heat exchanger in the presence of magnetic field, *Energy Conversion and Management*, 76 (2013) 1125–1133.

[24] M. Bahiraei, S.M. Hosseinalipour and M. Hangi, Numerical study and optimization of hydrothermal characteristics of Mn–Zn ferrite nanofluid within annulus in the presence of magnetic field, *J Supercond Novel Magn.*, 27(2), 527-534 (2020).

[25] M. Aneja, Sapna Sharma, S. Kuharat and O. Anwar Bég, Computation of electroconductive gyrotactic bioconvection under nonuniform magnetic field: Simulation of smart bio-nanopolymer coatings for solar energy, *Int. J. Modern Physics B,* 33, 2050028 (22 pages). (2020)

[26] Azizian R, Doroodchi E, McKrell T, Buongiorno J, Hu LW, Moghtaderi B., Effect of magnetic field on laminar convective heat transfer of magnetite nanofluids. *Int. J. Heat Mass Transf*. 68: 94–109 (2014).

[27] J.C. Umavathi, S.L. Patil, B. Mahanthesh and O. Anwar Bég, Unsteady squeezing flow of magnetized nano-lubricant between parallel disks with Robin boundary condition, *Proc. I MechE J. Nanomaterials, Nanoengineering and Nanosystems (2020).* DOI: 10.1177/23977914211036562

[28] M. Ferdows, F. Alzahrani, Study of non-isothermal incompressible flow and heat flux of nano ferro fluid with induced magnetic induction, *Int. Com. In Heat and Mass Trans*. 109, 104352 (2019).

[29] P. Ramesh Reddy, S. Abdul Gaffar, O. Anwar Bég, B. Md. Hidayathulla Khan, Hall and ionslip effects on nanofluid transport from a vertical surface: Buongiorno's model, *ZAMM- J. Applied Mathematics and Mechanics* (2021). DOI: 10.1002/zamm.202000174 (16 pages)

[24] W. Al-Kouz, A. Abderrahmane, M. Shamshuddin, O. Younis, S. Mohammed, O. Anwar Bég, D. Toghraie, Heat transfer and entropy generation analysis of water-Fe_3O_4/CNT hybrid magnetic nanofluid flow in a trapezoidal wavy enclosure containing porous media with the Galerkin finite element method, *European Physical Journal Plus* (2021). 136:1184 (23 pages)

[31] P. Sudarsana Reddy, P. Sreedevi, S. Venkateswarlu, Impact of modified Fourier's heat flux on the heat transfer of MgO/Fe_3O_4–Eg-based hybrid nanofluid flow inside a square chamber, *Waves in Random and Complex Media*, (2022), DOI: 10.1080/17455030.2022.2058112

[32] Dutz S, Clement JH, Eberbeck D, Gelbrich T, Hergt R, Müller R, Wotschadlo J, Zeisberger M., Ferrofluids of magnetic multicore nanoparticles for biomedical applications. *J Magn Magn Mater* 321:1501–1504 (2009).

[33] David SA, Veeraputhiran V, Vedhi C. Biosynthesis of cobalt oxide nanoparticles – a short review. *J Nanosci Technol*. 5:734–7 (2019).

[34] Vijayanandan AS, Balakrishnan RM. Photostability and electrical and magnetic properties of cobalt oxide nanoparticles through biological mechanism of endophytic fungus Aspergillus nidulans. *Appl Phys A Mater Sci Process*. 126:1 (2020).

[35] N. M. Al-Hada et al., Fabrication and characterization of Manganese–Zinc Ferrite nanoparticles produced utilizing heat treatment technique, *Results in Physics*, 12, 1821-1825 (2019).

[36] Akid, R., Wang, H., Smith, T. J., Greenfield, D., and Earthman, J. C. (2008). Biological functionalization of a sol–gel coating for the mitigation of microbial-induced corrosion. *Adv. Funct. Mater.* 18, 203–211 (2008).

[37] Ali, I. M., Ibrahim, I. M., Ahmed, E. F., and Abbas, Q. A. (2016). Structural and characteristics of manganese doped zinc sulfide nanoparticles and its antibacterial effect against gram-positive and gram-negative bacteria. *Open J. Biophys.* 6, 1–9 (2016).

[38] M. Lajvardi, J.M. Rad, I. Hadi, A. Gavili, T.D. Isfahani, F. Zabihi, J. Sabbaghzadeh, Experimental investigation for enhanced ferrofluid heat transfer under magnetic field effect, *J. Mag. Mag. Mater*. 322 (2010) 3508.

[39] Q. Li, Y. Xuan, Experimental investigation on heat transfer characteristics of magnetic fluid flow around a fine wire under the influence of an external magnetic field, *Exp. Therm. Fluid Sci.* 33 (2009) 591–596.

[40] P. Sreedevi, P. Sudarsana Reddy, Effect of magnetic field and thermal radiation on natural convection in a square cavity filled with TiO_2 nanoparticles using Tiwari-Das nanofluid model, *Alexandria Engineering Journal*, 61 (2), 1529-1541, (2022)

[41] Anum Shafiq, Tabassum Naz Sindhu, Chaudry Masood Khalique, Numerical investigation and sensitivity analysis on bioconvective tangent hyperbolic nanofluid flow towards stretching surface by response surface methodology, *Alexandria Engineering Journal*, 59 (6), 4533-4548, (2020).

[42] Shafiq, Anum , Mebarek-Oudina, Fateh & Sindhu, Tabassum & Abidi, Awatef, A study of dual stratification on stagnation point Walters' B nanofluid flow via radiative Riga plate: a statistical approach. The European Physical Journal Plus, 136(4), 1-24 (2021).

[43] hafiq, A., Sindhu, T.N. & Al-Mdallal, Q.M. A sensitivity study on carbon nanotubes significance in Darcy–Forchheimer flow towards a rotating disk by response surface methodology. *Sci Rep* 11, 8812 (2021).

[44] K.C. Cramer and S.I. Pai, *Magnetofluid Dynamics for Engineers and Applied Physicists*, MacGraw-Hill, New York, USA (1973).

[45] M. Kumari, H.S. Takhar, G. Nath, MHD flow and heat transfer over a stretching surface with prescribed wall temperature or heat flux, *Wäarme Stoffübertrag*. 25 (1990) 331–336.

[46] Y. Koshiba, T. Matsushita, M. Ishikawa, Influence of induced magnetic field on large scale pulsed MHD generator, in: *Proceedings of the 33rd Plasma Dynamics and Lasers Conference, AIAA, 20 - 23 May, Maui, Hawaii, USA* (2002).

[47] S.K. Ghosh, O. A. Beg, J. Zueco, Hydrodynamic free convection flow with induced magnetic field effects, *Meccanica*, 45 (2010) 175-185.

[48] T. Hayat, Anum Shafiq, A. Alsaidi, MHD axisymmetric flow of third grade fluid by a stretching cylinder. *Alexandria Engineering Journal*, 54(2), 205-212, (2015)

[49] Hayat, Tasawar & Qayyum, Sajid & Alsaedi, Ahmed & Shafiq, Anum. Inclined magnetic field and heat source/sink aspects in flow of nanofluid with nonlinear thermal radiation. International Journal of Heat and Mass Transfer, 103, 99-107 (2016), 10.1016/j.ijheatmasstransfer.2016.06.055.

[50] T. Hayat, Anum Shafiq, A. Alsaidi, S. Asghar, MHD axisymmetric flow of third grade fluid between stretching sheets with heat transfer. Computers & Fluids, 86, 103-108, (2013).

[51] T. Hayat, Anum Shafiq, A. Alsaidi, S. Asghar, Effect of inclined magnetic field in flow of third grade fluid with variable thermal conductivity. *AIP Advances*, 5(8), 087108, (2015)

[52] T. Hayat, Anum Shafiq, A. Alsaidi, Hydromagnetic boundary layer flow of Williamson fluid in the presence of thermal radiation and Ohmic dissipation. *Alexandria Engineering Journal*, 55(3), 2229-2240, (2016).

[53] A. Shafiq, S.A. Lone, T.N. Sindhu *et al.*, Statistical modeling for bioconvective tangent hyperbolic nanofluid towards stretching surface with zero mass flux condition. *Sci Rep* 11, 13869 (2021). https://doi.org/10.1038/s41598-021-93329-y

[54] O. Anwar Bég, D. Tripathi, T. Sochi and PK Gupta, Adomian decomposition method (ADM) simulation of magneto-biotribological squeeze film with magnetic induction effects, *J. Mechanics Medicine Biology*, 15, 1550072.1-1550072.23 (2015).

[55] O. Anwar Bég, Tasveer A. Bég, S.R. Munjam and S. Jangili, Homotopy and Adomian semi-numerical solutions for oscillatory flow of partially ionized dielectric hydrogen gas in a rotating MHD energy generator duct, *Int. J. Hydrogen Energy*, 46, 17677-17696 (2021).

[56] N. S. Akbar, D. Tripathi, Z. H. Khan and O. Anwar Bég, Mathematical model for ciliary-induced transport in MHD flow of Cu-H2O nanofluids with magnetic induction, *Chinese J. Physics, 55. 947-962 (2017).*

[57] O. Anwar Bég, M. Ferdows, Shamima Islam and M. Nazrul Islam, Numerical simulation of Marangoni magnetohydrodynamic bio-nanofluid convection from a non-isothermal surface with magnetic induction effects: a bio-nanomaterial manufacturing transport model, *J. Mechanics Medicine Biology*, 14, 3, 1450039.1-1450039.32 (32 pages) (2014).

[58] M.R. Bin Mizwan, M.A. Ferdows, M.D. Shamshuddin, O. Anwar Bég, S. Sulyman and A. Kadir, Computation of ferromagnetic/non-magnetic nanofluid flow from a stretching cylinder with induction and curvature effects, *Heat Transfer*, 50, 5240-5266 (2021).

[59] Shahina Akter, M. Ferdows, Tasveer A. Bég, O. Anwar Bég Ali Kadir, S. Sun, Spectral relaxation computation of electroconductive nanofluid convection flow from a moving surface with radiative flux and magnetic induction, *J. Computational Design & Engineering*, 8(4), 1158–1171 (2021).

[60] M. J. Uddin, M.N. Kabir, O. Anwar Bég and Y. Alginahi, Chebyshev collocation computation of magneto-bioconvection nanofluid flow over a wedge with multiple slips and magnetic induction, *Proc. IMechE: Part N-Journal of Nanomaterials, Nanoengineering and Nanosystems*, 232, 109-122 (2018).

[61] O. Anwar Bég, S. Kuharat, M. Ferdows, M. Das, A. Kadir, M. Shamshuddin, Magnetic nano-polymer flow with magnetic induction and nanoparticle solid volume fraction effects: *solar magnetic nano-polymer fabrication simulation, Proc. IMechE-Part N: J Nanoengineering, Nanomaterials and Nano-systems* (2019). DOI: 10.1177/ 2397791419838714 (19 pages)

[62] T. Hayat, M. Farooq, A. Alsaedi, Homogenous-heterogeneous reactions in the stagnation point flow of carbon nanotubes with Newtonian heating, *AIP Adv*. 5 (2015) (027130–18).

[63] T. Hayat, K. Muhammad, M. Farooq, A. Alsaedi, Melting heat transfer in stagnation point flow of carbon nanotubes towards variable thickness surface, *AIP Adv*. 6 (2016) 015214–015216.

[64] Q.Z. Xue, Model for thermal conductivity of carbon nanotube-based composites, *Physica B: Condensed Matter*, 368, 302-307 (2005).

[65] Shampine, L.F., and J. Kierzenka., A BVP Solver based on residual control and the MATLAB PSE, *ACM Trans. Math. Softw.* 27 (3) (2001) 299–316.

[66] Z. Iqbal, E. Azhar, E. N. Maraj, Transport phenomena of carbon nanotube and bioconvection nanoparticles on stagnation point flow in presence of induced magnetic field, *Physica E*, 91 (2017) 128-135.

[67] B. J. Gireesha, B. Mahanthesh, I. S. Shivakumara, K. M. Eshwarappa, Melting heat transfer in boundary layer stagnation point flow of nanofluid toward a stretching sheet with induced magnetic field, *Eng. Sci. Tech.- Int. Jour*. 19(2016) 313-321.

[68] F.S. Ibrahim, M.A. Mansour, M.A.A. Hamad, Lie-group analysis of radiation and magnetic field effects on free convection and mass transfer flow past a semi-infinite vertical flat plate, *Electronic J. of Diff. Eqns*. 2005 (2005) 1–17.

[69] S. Mukhopadhyay, G.C. Layek, S.A. Samad, Study of MHD boundary layer flow over a heated stretching sheet with variable viscosity, *Int. J. Heat Mass Transfer*, 48 (2005) 4460–4466.

[70] R. Kandasamy, I. Muhaimin, Scaling transformation for the effect of temperature-dependent fluid viscosity with thermophoresis particle deposition on MHD-free convection heat and mass transfer over a porous stretching surface. *Transp. Porous Media*, 84 (2010) 549-565.

[71] I. Muhaimin, R. Kandasamy, I. Hashim, Scaling transformation for the effect of chemical reaction on free convection heat and mass transfer in the presence of variable stream conditions. *Chem. Eng. Res. and Design*, 88(10) (2010) 1320-1328.

[72] M.A.A. Hamad, I. Pop, Scaling transformations for boundary layer stagnation-point flow towards a heated permeable stretching sheet in a porous medium saturated with a nanofluid and heat absorption/generation effects, *Transp. Porous Media*, 87 (2011) 25-39.

[73] Z. Iqbal, E. Azhar, E. N. Maraj, Transport phenomena of carbon nanotube and bioconvection nanoparticles on stagnation point flow in presence of induced magnetic field, *Physica E*, 91 (2017) 128-135.

[74] MD. Shamshuddin, S.O. Salawu, O. Anwar Bég, T. A. Bég and Ali Kadir, Computation of reactive mixed convection radiative viscoelastic nanofluid thermo-solutal transport from a stretching sheet with Joule heating, *International Journal of Modelling and Simulation* (2021). DOI: 10.1080/02286203.2021.2012635 (26 pages)

[75] G. Kumaran, R Sivaraj, V. Ramachandra Prasad, O. Anwar Bég, Numerical study of axisymmetric magneto-gyrotactic bioconvection in non-Fourier tangent hyperbolic nano-functional reactive coating flow of a cylindrical body in porous media, *European Physical Journal Plus*, 136, 1107 (2021). https://doi.org/10.1140/epjp/s13360-021-02099-z